nature astronomy

Article

https://doi.org/10.1038/s41550-025-02659-8

Catastrophic disruption of asteroid 2023 CX1 and implications for planetary defence

Received: 22 January 2025

Accepted: 11 August 2025

A list of authors and their affiliations appears at the end of the paper

Mitigation of the threat from airbursting asteroids requires an understanding of the potential risk they pose for the ground. How asteroids release their kinetic energy in the atmosphere is not well understood due to the rarity of large impacts. Here we present a comprehensive, space-to-laboratory characterization of an impact of an L chondrite, which represents a common type of Earth-impacting asteroid. Small asteroid 2023 CX1 was detected in space and predicted to impact over Normandy, France, on 13 February 2023. Observations from several independent sensors and reduction techniques revealed an unusual but potentially high-risk fragmentation behaviour. The nearly spherical 650 ± 160 kg (72 ± 6 cm diameter) asteroid catastrophically fragmented at a dynamic pressure of 4 MPa around 28 km altitude, releasing 98% of its total energy in a concentrated region of the atmosphere. The resulting shock wave was spherical, not cylindrical, and released more energy closer to the ground. This type of fragmentation increases the risk of substantial damage at ground level. These results warrant consideration for a planetary defence strategy for cases where a >3–4 MPa dynamic pressure is expected, including planning for evacuation of areas beneath anticipated disruption locations.

Energetic airbursting asteroid impacts, such as the 500 kt of TNT equivalent Chelyabinsk event in February 2013[1], are exceedingly rare, leaving considerable uncertainty about the altitude of energy deposition by different asteroid types. Among the most dangerous deeply penetrating asteroids are those in the S and Q classes, which deliver ordinary chondrite meteorites. These meteorites are classified into H, L and LL groups based on petrographic characteristics and distinct parent bodies. L chondrites are the most commonly recovered from observed falls[2], making them one of the most frequently impacting asteroid types.

On 12 February 2023, a small asteroid approaching Earth was discovered by the Piszkéstető station of the Konkoly Observatory in Hungary[3]. Designated 2023 CX1, the asteroid was predicted to impact 6.7 h later over Normandy, France. Prompt alerts from the European Space Agency and NASA were quickly shared by the International Meteor Organization as well as by the Fireball Recovery and InterPlanetary Observation Network (FRIPON) and its citizen science counterpart Vigie-Ciel[4,5]. The rapid mobilization of these networks enabled a large-scale, coordinated effort to observe the fireball. A comprehensive dataset of optical, radio, infrasound and seismic measurements was collected during the atmospheric entry of the meteoroid at 02:59 UTC on 13 February.

Thanks to rapid data analysis and the exceptional mobilization of the public through the FRIPON/Vigie-Ciel network, a coordinated ground search led to the recovery of the first 93-g meteorite just 2 days after the fall, near the village of Saint-Pierre-le-Viger in Normandy[6,7]. The meteorite was named after this village and is hereafter referred to as SPLV. It is classified as an L5-6 chondritic breccia based on mineralogical and petrographic features, including an olivine Fa content of 24.6–26.5, low-Ni sulfides (<0.5 wt%), orthorhombic low-Ca pyroxene, limited olivine variation (<5%) and a scarcity of chondrules in thin sections. Shock indicators, such as undulatory extinction, weak mosaicism and planar fractures in olivine, and abundant shock veins support a shock stage of S3 (ref. 8). Further mineralogical details are provided in ref. 9.

Comprehensive investigations of asteroid impacts combining pre-impact observations, atmospheric fragmentation analysis and

e-mail: auriane.egal@montreal.ca

Table 1 | Orbital parameters and atmospheric entry location of 2023 CX1, determined from telescopic asteroid observations before impact (JPL 13) and from in-atmosphere meteor data

Symbol	Parameter	Telescopic (JPL 13)	In atmosphere	Combined (JPL 14)
e	Eccentricity	$0.434567\pm1\times10^{-5}$	$0.4369\pm2\times10^{-3}$	$0.4345664\pm6\times10^{-6}$
a	Semimajor axis (au)	$1.629319\pm4\times10^{-5}$	$1.6356\pm6\times10^{-3}$	$1.629318\pm1\times10^{-5}$
q	Perihelion distance (au)	$0.9212712\pm2\times10^{-6}$	$0.92106\pm5\times10^{-4}$	$0.92127115\pm8\times10^{-7}$
i	Inclination (°)	$3.41838\pm1\times10^{-4}$	$3.430\pm3\times10^{-2}$	$3.418380\pm4\times10^{-5}$
Ω	Longitude of ascending node (°)	$323.8709587\pm5\times10^{-6}$	$323.87032\pm9\times10^{-4}$	$323.8709589\pm2\times10^{-6}$
ω	Argument of perihelion (°)	$218.78816\pm2\times10^{-4}$	$218.779\pm7\times10^{-2}$	$218.788170\pm7\times10^{-5}$
m	Mean anomaly (°)	$316.5723\pm1\times10^{-3}$	$316.84\pm2\times10^{-1}$	$316.57224\pm6\times10^{-4}$
ϕ	Latitude (°N)	$49.921614\pm1\times10^{-4}$	$49.92182\pm2\times10^{-4}$	$49.921654\pm6\times10^{-5}$
λ	Longitude (°E)	$-0.167195\pm4\times10^{-4}$	$-0.16713\pm2\times10^{-4}$	$-0.167172\pm1\times10^{-4}$
H	Altitude (km)	101.755 ± 0.00	101.755 ± 0.00	101.755 ± 0.00
t	Time on 13 February (UTC)	02:59:13.20±0.05	02:59:13.23±0.05	02:59:13.21±0.03

The combined solution (JPL 14) incorporates telescopic data anchored by the atmospheric entry point derived from meteor observations. The orbital elements are for an osculating epoch of 14.0 December 2022 TDB, that is, 60 days before impact and before substantial perturbation by Earth's gravity. The location of the meteoroid at a fixed reference altitude of 101.755 km, corresponding to the first observed position of the fireball, is provided for each orbital solution.

geochemical studies of recovered meteorites remain rare. To date, only 11 asteroids have been detected before impact. Among them, just four led to meteorite recovery, and detailed atmospheric observations are lacking in most cases. SPLV is the only L chondrite linked to a pre-impact detection. Here we present a multi-disciplinary analysis of SPLV, combining telescopic measurements, fireball observations, precise meteorite recovery and laboratory analyses to investigate how L-chondrite asteroids fragment and deposit energy in Earth's atmosphere.

Results

Asteroid orbit, shape and size

Orbit. Between 20:18 UTC on 12 February and 02:52 UTC on 13 February, 22 astronomical observatories reported observations of 2023 CX1 to the Minor Planet Center (MPC). High-fidelity orbit determination based on precise tracking of the asteroid enabled the prediction of the impact time to within a few seconds. Targeted observations of the fireball allowed for a detailed comparison between the telescopic and fireball-derived orbits by examining their relative positions at the top of the atmosphere. Initially, a notable offset of about 90 m was observed between the predicted impact location and the first fireball detection at an altitude of 101.755 km. A thorough analysis of the measurements revealed that the primary source of error stemmed from the confusion between WGS84 and mean sea level elevations of the station coordinates reported by the observers to the MPC. After correcting the coordinates, the position of the asteroid at the reference altitude, derived from both telescopic and fireball observations, differed by less than 30 m, well within 1σ uncertainties (Table 1 and Extended Data Fig. 1). This strong agreement enabled a cross-calibration between telescopic and fireball data, reducing the final relative offset between the trajectories at the reference altitude to approximately 18 m (Table 1), and establishing SPLV as having one of the most precise meteorite orbits ever measured.

Asteroid shape. Photometric measurements of 2023 CX1 were conducted as the asteroid approached Earth between 23:30 UTC and 02:51 UTC on the night of 12–13 February. These observations produced a nearly flat light curve with variations of ±0.3 mag centred around an absolute magnitude of 32.7 (Extended Data Fig. 2). The possible weak periodicity of 18.33 s indicated in ref. 10 was not identified in any of our datasets. The lack of notable periodicity in the asteroid light curve, despite a high temporal resolution of ~2 s, indicates that 2023 CX1 was either nearly spherical in shape or a fast rotator with a period below 2 s.

Mass and size. A complete characterization of the fireball was performed using optical and seismo-acoustic observations. In addition to the various photographic and video records of the fireball, the atmospheric entry of 2023 CX1 generated an infrasound signal that was detected as far as ~5,500 km away in Russia and as close as Flers, Normandy, within 150 km of the fall.

Additionally, six SPLV fragments were sent for petrographic and cosmochemical analysis shortly after their recovery. These included noble gas measurements, non-destructive gamma spectrometry (GS) and destructive instrumental accelerator mass spectrometry (IAMS). The bulk rock chemical composition of the meteorite, determined from one SPLV sample, is provided in Supplementary Table 3. Photogrammetry models and laser scans, which provided independent volume measurements of four SPLV meteorites, resulted in average bulk densities of 3.353 ± 0.080 g cm^{-3} and 3.294 ± 0.002 g cm^{-3}, respectively ('Meteorite density'). An average bulk density of 3.3 g cm^{-3} was assumed for the rest of the analysis.

We estimated the pre-atmospheric size and mass of 2023 CX1 using seven independent methods, including telescopic observations before impact, fireball measurements and laboratory analyses of cosmogenic nuclides in recovered meteorites ('Pre-atmospheric radius and mass'). The initial radius estimate of 40–85 cm (ref. 10), based on the absolute magnitude and assumed albedo of the object, was further refined using optical fireball observations, energy deposition modelling from seismo-acoustic data and concentrations of cosmogenic nuclides. Each method provided constraints on the pre-atmospheric radius, which converge towards a preferred value of 36 ± 3 cm and a total mass of 650 ± 160 kg (Extended Data Table 1).

Asteroid behaviour in Earth's atmosphere

The fireball trajectory was determined from photographs and videos captured at 12 different sites across France, the Netherlands and the UK. The targeted high-resolution observations by the general public proved crucial for an accurate determination of the trajectory ('Meteor optical analysis'). The fireball was first detected at an altitude of 101.755 km at 02:59:13.22 UTC and tracked for 9.17 s down to 18.91 km.

The fireball light curve is shown in Fig. 1. Its brightness increased gradually over the first 4 s, corresponding to the heating-up phase of the body before vigorous ablation starts[11]. The brightness then nearly plateaued at an absolute magnitude of −12 during 3 s, before a bright double-peaked flare occurred, signalling two main fragmentation events at altitudes of 29.4 km and 27.1 km. At the peak, the brightness increased by 3.5 mag (a 25-fold increase), reaching a maximum absolute

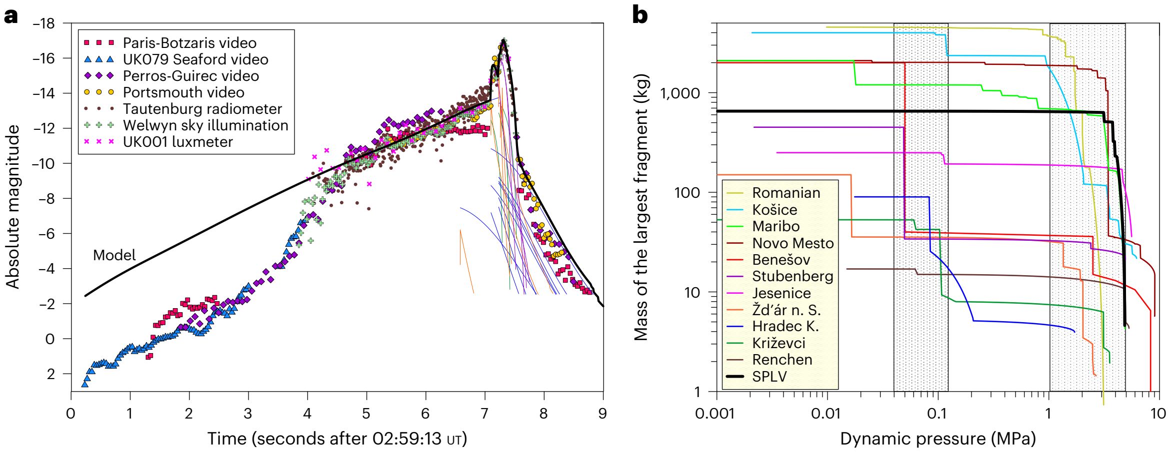

Fig. 1 | Fireball light curve and modelled fragmentation behaviour. **a**, Meteor light curve expressed in visual magnitude from a distance of 100 km. Symbols indicate data from different instruments. The modelled light curve is shown as a black line. Coloured lines represent the modelled contributions of individual fragments and dust released from the meteoroid, as detailed in ref. 14. **b**, Modelled mass of the largest surviving fragment of the SPLV meteorite as function of increasing dynamic pressure. Results are compared with the fireballs of meteorites Novo Mesto[28] (L5), Benešov (LL3.5-H5), Hradec Králové (LL5), Stubenberg (LL6), Košice (H5), Križevci (H6), Renchen (L5-6), Jesenice (L6), Žďár nad Sázavou (L3), Maribo (CM2) and the 7 January 2015 superbolide observed over Romania[14,26]. Grey areas indicate the two distinct ranges of dynamic pressures at which decimetre-sized ordinary chondrites fragment[14].

magnitude of −17 at 02:59:20.32 UT, corresponding to a fragmentation event under a dynamic pressure of 4 MPa. As in previous studies (for example, refs. 11–14), we assume that fragmentation occurs when the dynamic pressure, which depends on both velocity and atmospheric density, exceeds the internal strength of the body.

The light curve and the deceleration of the main body and fragments were modelled using the semi-empirical fragmentation model of ref. 14, assuming a meteoroid density of 3.3 g cm^{-3} and a luminous efficiency of 4% ('Meteor optical analysis'). The model accurately reproduced the light curve before and after the flare, except for the pre-heating phase that was excluded from the fit.

Both the light curve and the deceleration indicate that no considerable fragmentation occurred before the flare. From the bolide observations, the computed initial mass of the meteoroid of 650 ± 160 kg (in good agreement with the other independent measurements listed in Extended Data Table 1) decreased to 630 kg just before the flare. The flare itself marked the near-total destruction of 2023 CX1 (Fig. 1). It broke into small fragments and dust, which quickly evaporated. This behaviour is unique among almost all other meteorite falls, which generally fragment and lose most of their mass at low dynamic pressures (<0.12 MPa; Fig. 1).

At least nine individual fragments were identified in the most detailed video recorded from the village La Fresnaye, with their estimated masses listed in Extended Data Table 2. One relatively large fragment (F), which lagged further behind the main mass, probably separated from the meteoroid before the flare at an altitude of about 35 km and time 6.6 s (02:59:19.6 UT). As no brightness increase was observed at that altitude, no substantial dust release and only minimal mass loss occurred during the fragmentation.

All the other individual fragments were produced during the double-peaked flare. Three large stones (A, D and I) separated during the first fragmentation event at 29.4 km altitude, and five others were released during the second, more prominent fragmentation phase around 28.1 km. The separation of the largest fragment observed (A) at the onset of the flare caused a notable deceleration and a change in the direction of the meteoroid of about ~0.8° (1.2° southwards in azimuth and 0.3° downwards in slope; Extended Data Table 3). The motion of fragment A was fitted best with an elevated ablation coefficient of 0.015 ± 0.003 kg MJ^{-1} (three times the baseline; 'Meteor optical analysis'), indicating possible further fragmentation between the flare and the end of the fireball.

A seismo-acoustic analysis of the atmospheric entry indicates that most of the kinetic energy of the body was released at once during the flare. The arrival times of the resulting acoustic shock wave at seismic stations within 150 km of the source were used to independently estimate the location of the fragmentation event (Extended Data Tables 4 and 5 and 'Seismo-acoustic analysis of the meteor'), confirming the position derived from optical observations (Extended Data Table 2).

Fragment distribution on the ground

The meteorite strewn field is presented in Fig. 2. More than 100 meteorites totalling a mass of 1.34 kg (~0.2% of the initial mass of the meteoroid) were recovered along a distance of 8 km. All retrieved fragments have a fusion crust, indicating that they separated from the meteoroid during ablation (while travelling at speeds exceeding ~4 km s^{-1}) and did not subsequently break. The location and mass of the reported stones, ranging from <1 g to 490 g, are shown in Fig. 2 and listed in Supplementary Table 1.

Several modelling approaches were used to investigate the meteorite strewn field, with details provided in 'Strewn-field modelling'. Individual fragments identified in the video records after the flare were modelled to estimate the landing locations of the largest meteorites (red circles). Our results indicate that the three largest stones recovered were found near the predicted locations of fragments B, G and F, whereas the largest expected stone (~1.5 kg, corresponding to fragment A) has not yet been recovered.

Stone 4, found farther north, can be explained by a 5° northwards deviation at the main flare (orange circles in Fig. 2), which occurred when fragment A deviated southwards. Another possibility is that this meteorite separated from fragment A near the trajectory end point and experienced a strong drag afterwards. However, no further fragmentation was observed in the fireball records, hampering the confirmation of late-stage fragmentation. Deviations of 1° to 5° northwards also reproduce the concentration of fragments recovered south-east of Angiens (near fragments 10 and 13). The absence of recovered meteorites in the southern part of the strewn field may be due to less thorough searches in that area. Most of the small meteorites north of Angiens lie within 400 m of the central line (blue-shaded areas). The northernmost fragments align well with high-drag scenarios, involving ejection of elongated meteorites at the flare ('Strewn-field modelling').

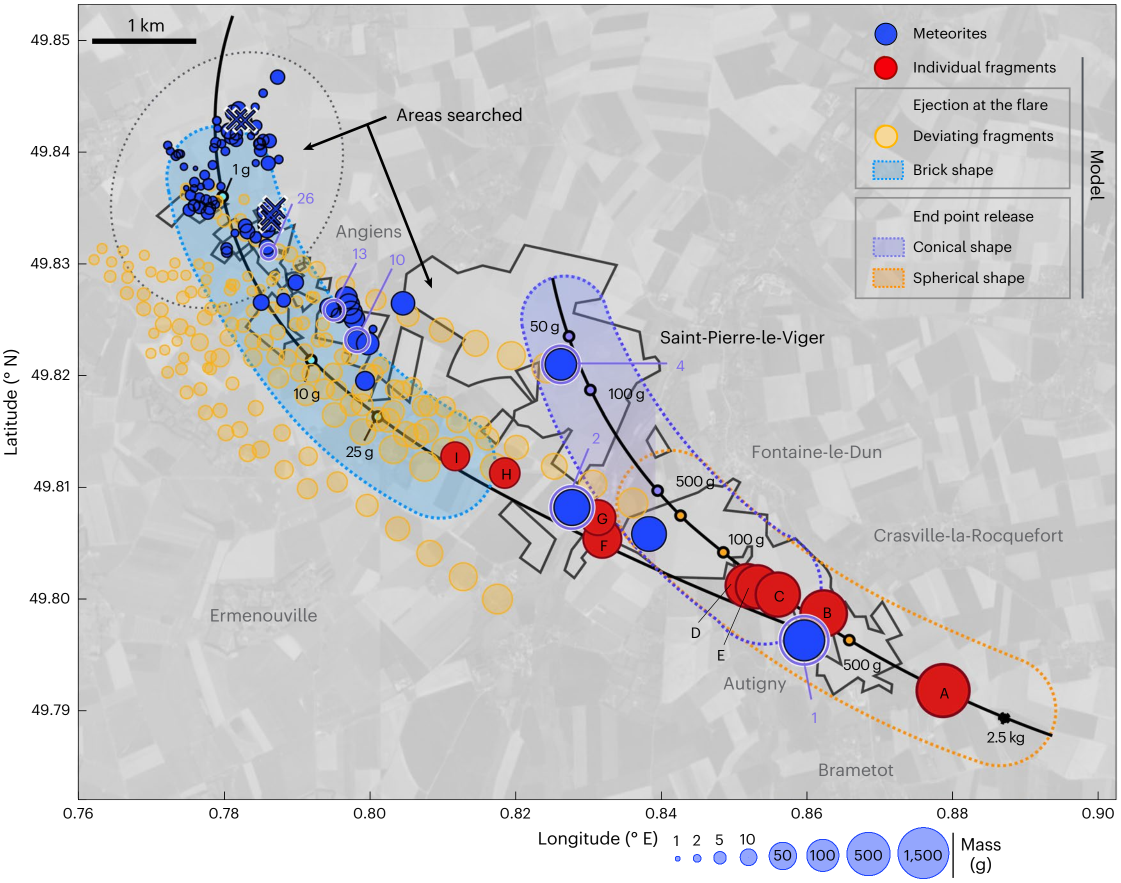

Fig. 2 | Strewn field of SPLV. Recovered meteorites are shown in blue. Circle sizes correspond to the mass of modelled or collected fragments, ranging from 1 g to 1.55 kg. Meteorites with known coordinates but uncertain masses are indicated by blue crosses. The positions of the stones sent for cosmogenic nuclide analysis are highlighted in purple. Red circles show the calculated fall location of the nine individual fragments identified in the video recorded from La Fresnaye. Orange circles represent the hypothetical locations of small fragments released at the main flare, with up to 5° deviation in all directions from the original trajectory. The blue-shaded area indicates the landing sites of brick-shaped fragments weighing less than 50 g, which were ejected during the main fragmentation event. Orange and purple regions show the predicted landing zones for larger fragments with conical (purple) and spherical (orange) shapes, modelled from the end point of the visible trajectory. The most intensively searched areas, where documented, are shaded in grey. Credit: Background map from Google Earth Data SIO, NOAA, U.S. Navy, NGA, GEBCO, Image Landsat/Copernicus.

Further insight into the fragmentation process was sought from cosmogenic nuclide studies. In well-measured past falls (for example, ref. 15), most of the central part of the meteoroid fragmented first, while the near-surface backside of the meteoroid survived longer and fell as larger fragments on the ground at the head of the strewn field. For SPLV, however, we observe no correlation between the ^{60}Co activity of the samples, which increases with shielding depth, and their position in the strewn field (Supplementary Table 4). Measured $(^{21}\mathrm{Ne}/^{22}\mathrm{Ne})_{\mathrm{cos}}$ ratios were used as a shielding indicator also, where subscript 'cos' represents cosmogenic. An upper limit for the pre-atmospheric radius of 50 cm (based on estimates in Extended Data Table 1) was applied to better constrain the production rates of cosmogenic nuclides. Consistent $(^{21}\mathrm{Ne}/^{22}\mathrm{Ne})_{\mathrm{cos}}$ ratios were determined for all analysed samples (Extended Data Table 6), and similar shielding depths of 21–40 cm were measured for stones at the beginning (26), middle (10) and end (4) of the strewn field. Variations in ^{26}Al concentrations measured by both IAMS and GS show no notable trend along the strewn field. Although the two techniques yield slightly divergent values ('Instrumental accelerator mass spectrometry'), both datasets consistently indicate that there is no correlation between the shielding depth of the samples and their position within the field. This supports the sudden disruption of 2023 CX1, which led to the dispersion of fragments from both the interior and surface of the meteoroid across the strewn field.

Meteorite geochemistry and origin

Owing to the short observation window before impact, no telescopic reflectance spectra could be obtained for 2023 CX1. However, the combination of its well-constrained orbit and the comprehensive geochemical analyses of the recovered meteorites provides critical insights into its origin.

2023 CX1 has a Lyapunov time of 50–100 years, typical of near-Earth asteroids[16], indicating a highly chaotic orbit that limits reliable predictions beyond a few centuries. However, the backwards integration of clones representing the error ellipse of combined telescopic and meteor data indicates a 90% probability that 2023 CX1 was in near-Earth space ($q < 1.3$ au) 1 Myr ago and an 80% probability 10 Myr ago. Over the past 10 Myr, the clones spent 75% of their time within the inner main belt ($1.3 < a < 2.5$ au) and about 1% in the Hungaria region ($1.76 < a < 2.00$ au, $16° < i < 34°$), consistent with an origin as an inner main belt asteroid.

Gas retention ages, measured by the U/Th–He (T_4) and K–Ar (T_{40}) thermochronometers, were used to trace the thermal history of the meteoroid in its parent body. These ages were notably consistent across the five SPLV samples analysed (Extended Data Table 7). T_{40} values indicate gas retention since 4.3–4.6 Gyr ago for SPLV, consistent with its formation. The younger T_4 ages, clustering around 2.4–2.8 Gyr, indicate one or several minor resetting events (for example, impacts) experienced by the parent body. The $T_{4,40}$ ages do not show a signature

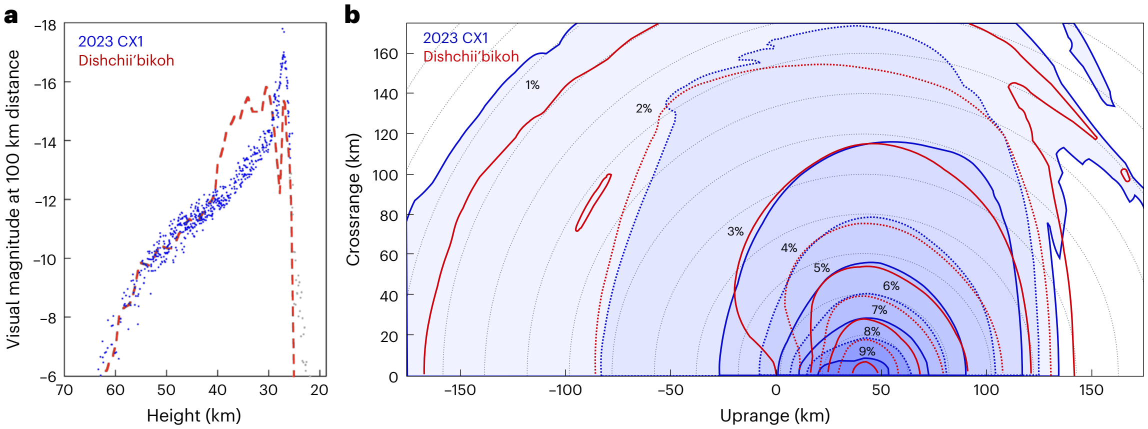

Fig. 3 | Energy deposition and ground-level overpressure for 2023 CX1 and Dishchii'bikoh. a, Energy deposition profile (on a logarithmic scale) of 2023 CX1 compared with the more common profile of Dishchii'bikoh[29]. **b**, Ground-level overpressure profiles generated by a gradually fragmenting body (Dishchii'bikoh) and an abruptly disrupting one (2023 CX1), for an impact energy of 18 Mt. Contours mark overpressure levels in percent.

of the break-up event of the main parent body around 466 Myr, as recorded in ~50% of L-chondrite meteorites[17].

Cosmic-ray exposure (CRE) ages, used to determine the time of ejection from the parent body[18], are also largely consistent across all SPLV samples analysed. CRE ages determined from the ^{21}Ne abundance, more reliable than based on the ^{3}He and ^{38}Ar concentrations, indicate a preferred value of 27–32 Myr for SPLV (Extended Data Table 7) which is consistent with other L chondrites (for example, ref. 19). T_{26} ages determined from the ^{26}Al–^{21}Ne isotope pair method[20] yield similar estimates around a weighted average of 30 ± 3 Myr.

The CRE age and orbital characteristics of SPLV are fully consistent with the suggestion that L chondrites originate from the Massalia family, an S-type asteroid group in the inner main belt. In particular, dynamical analyses using the METEOMOD model[21] indicate an ~94% probability that 2023 CX1 originated from a subpopulation of this family (identified as Massalia$_2$), formed by a cratering or reaccumulation event on asteroid (20) Massalia 30–40 Myr ago (refs. 21,22). The object was most probably delivered to Earth due to the ν_6 resonance (Extended Data Fig. 3 and Supplementary Table 7). According to collisional simulations in ref. 21, this family has the potential to deliver 10 to 20 one-meter-sized impactors to Earth every year.

Discussion

2023 CX1 lost approximately 98% of its mass during a single catastrophic disruption. With fragmentation stopping nearly instantaneously, almost all its kinetic energy was deposited as a point source at around 28 km in altitude when the dynamic pressure reached 4 MPa. Such behaviour is highly atypical for common smaller meteorite-dropping fireballs, although the number of well-characterized and modelled metre-sized impactors is only ~10. Most smaller chondritic meteorite-dropping fireballs exhibit two distinct fragmentation phases: an early loss of mass at low dynamic pressures (below 0.12 MPa), sometimes followed by moderate to severe fragmentation deeper in the atmosphere (1–5 MPa)[13,14]. 2023 CX1 did not undergo substantial fragmentation at low dynamic pressures, unlike all the 22 meteorite-dropping fireballs analysed in ref. 14.

We identified four other events in which asteroids resisted disruption to as high pressures as 2023 CX1. One of the Prairie Network fireballs[23] survived up to 5 MPa without breaking apart, but data for this event are sparse. The Carancas impactor, an H4-5 chondrite that formed a 13-m crater in Peru, may have reached the ground mostly intact[24], but no unique trajectory could be derived from its infrasound and seismic signals[25]. In January 2015, a metre-sized asteroid entered over Romania and resisted pressures up to 0.9 MPa before losing ~90% of its mass through several fragmentations up to 3 MPa; no meteorites were recovered[26].

The most similar case to 2023 CX1 is Novo Mesto, which entered over Slovenia on 28 February 2020[27,28]. It suddenly disrupted at 35 km altitude, losing more than 80% of its mass around 3 MPa. The meteoroid generated a 0.3-kt airburst that was detected as a minor earthquake on the ground, and it dropped heavily shocked L5 chondrites. Like 2023 CX1, Novo Mesto has been found to have a ~96% probability of originating from the Massalia$_2$ family, according to the METEOMOD model (Supplementary Table 7).

This fragmentation behaviour is not due to the impactors being homogeneous monoliths with little or no residual damage from past collisions, as observed for the Carancas event[24]. The dynamic pressure at break-up is at least an order of magnitude lower than that measured for recovered L-chondrite meteorites[14]. Both Novo Mesto and 2023 CX1 exhibit numerous shock veins, and computed tomography of SPLV fragments revealed macroscopic fractures probably formed by past collisional processing on the parent body.

Compared with gradually fragmenting bodies of similar size, disrupting asteroids are expected to deposit more energy closer to the ground. To investigate this effect, we compared 2023 CX1-like fragmentation to that of Dishchii'bikoh[29], an LL chondrite of comparable size, entry angle and velocity, which exhibited a more gradual fragmentation process (Fig. 3). Hydrocode simulations were conducted for both fragmentation regimes, assuming an 18-Mt energy release (equivalent to the Tunguska impactor[30]), to isolate the effect of fragmentation style on shock-wave propagation. Although absolute overpressures scale with impact energy, the relative differences in the resulting ground footprint remain valid for lower energy events such as 2023 CX1 (see 'Blast-wave pressure calculations' in Methods for details).

Notable differences in ground-level effects are observed between the two fragmentation scenarios (Fig. 3). The abrupt fragmentation of SPLV generates a more spherical shock wave compared with the cylindrical shock wave in a normal entry, concentrating more energy uprange and crossrange with a deficit downrange. As a result, the area affected by high overpressures increases substantially (by a factor of 4 at 9%) compared with a typical entry. Differences vanish only at large distances (>100 km), where the source becomes effectively point-like. The closer the blast occurs to the ground, the more pronounced these differences will be, particularly at higher overpressures. Shallow entry angles will also further enhance this effect, as the cylindrical shock wave becomes more downward directed, increasing the downrange impact.

These findings point to a class of L-chondrite-like asteroids capable of producing disproportionately large airbursts for their size, as postulated in ref. 28. By releasing most of their energy in a single catastrophic disruption, such objects would probably cause greater ground-level damage than gradually fragmenting bodies of similar size (for example, Chelyabinsk[31]). The fragmentation behaviour observed for 2023 CX1 is consistent with the second fragmentation regime identified in other L-chondrite falls[14], indicating that similar responses may be expected among other damaged yet cohesive bodies from this group.

The potential for sudden and concentrated energy release among L-chondrite-like asteroids, possibly linked with the Massalia family, must, therefore, be considered when assessing the impact threat from S- and Q-class asteroids. In addition to the high-precision orbital tracking deployed to observe 2023 CX1, planetary defence strategies should prioritize spectral measurements of incoming objects. Pre-impact detections pointing to a probable L-chondrite-like asteroid should warrant enhanced public notification and consideration of evacuation for areas beneath the predicted fragmentation location.

Methods

Asteroid astrometry

Most astrometric measurements used in the trajectory determination were extracted by the original observers and reported to the MPC. The pre-impact trajectory was based on 368 observations collected before the body entered Earth's shadow. Key observations were strategically prioritized by the European Space Agency to optimize trajectory accuracy in both spatial and temporal domains. Early night prioritization of observations from distant locations (K91 in South Africa and V39 in the United States) and the Catalina Sky Survey (703) enabled essential parallax measurements. Precise time anchoring for trajectory determination was provided by observations from Rantiga, Italy (D03), using a GPS-synchronized CMOS camera calibrated to global navigation satellites with at least 20-ms accuracy, predicting impact location and timing within 400 m and a few seconds.

The post-impact analysis involved recalibrating the astrometry from several observatories, including Višnjan (L01), Satino (C95), Dax (958), Conques (I93), Berthelot (L54) and Piszkéstető (K88), applying proper trail-fitting techniques and verifying timing and geographic coordinates. Numerous errors in the coordinates reported to the MPC by observers required corrections. Notably, about 55% of the altitudes reported as above the ellipsoid (WGS84) actually referred to heights above mean sea level, with discrepancies reaching up to 95 m.

Asteroid photometry

Photometric reductions of the L01, L54 and I93 station data were performed using standard procedures[32], including bias subtraction and flat-field correction. Photometry was measured and calibrated using the Photometry Pipeline[33]. The Gaia Data Release 2 reference catalogue[34] and Pan-STARRS Data Release 1 catalogue[35] were used for astrometric and photometric calibrations, respectively. In general, only those datasets where the signal-to-noise ratio per exposure of 2023 CX1 was greater than ~2 were selected for the light-curve analysis. All light-curve data were collected shortly before impact when the viewing geometry to 2023 CX1 was changing markedly. The photometry was, thus, corrected for range (heliocentric and geocentric) and phase angle. These corrections were applied assuming a standard H-G photometric model[36], an absolute magnitude $H = 32.76$ and geometry parameters retrieved from the JPL Horizons system. Photometric reductions of the K88 station data were performed using the tasks in the software FITSH (ref. 37). C65 observations were conducted over a 45-min interval beginning at 23:30 UT on 12 February 2023, employing continuous 5-s exposures through a Johnson–Cousins R filter. The images were reduced using the ICAT analysis tool[38]. Finally, high-resolution temporal measurements of the magnitude variations of the asteroid were obtained from observations at the Schiaparelli Observatory (204), with an effective exposure time of 0.25 s during 60-s observation windows. Photometric reductions were performed using the Astrometrica software[39]. Searches for periodicity in the brightness variations of the asteroid were conducted across datasets L01, L54, C65, I93, K88 and 204. No notable periodicity was identified in any of the datasets, including the I93 observations, which had a temporal resolution of ~2 s.

Pre-atmospheric radius and mass

The pre-atmospheric radius and mass of 2023 CX1 were independently determined from asteroid photometry, optical and seismo-acoustic analyses of the fireball and cosmogenic nuclide measurements of SPLV samples. These estimates, summarized in Extended Data Table 1, assume a spherical shape and an average bulk density of 3,300 kg m^{-3} measured for SPLV. Geometric albedos were computed from the absolute magnitude and estimated size of the asteroid using the standard photometric model in ref. 36.

Initial radius estimates based on the absolute magnitude of the asteroid of 32.7 ± 0.3 ranged from 40 cm to 85 cm (ref. 10). Unfortunately, no reflectance spectra or direct albedo measurements were obtained before impact, preventing a firm constraint on the size of the body from photometry alone. However, L chondrites have long been linked to S-type asteroids[40,41]; in particular, 2023 CX1 is suspected to originate from the Massalia family ('Meteorite geochemistry and origin' in 'Results'), whose members exhibit L-chondrite-like compositions[22]. From the Virtual Observatory Solar System Open Database Network[42], we derived a geometric albedo of 0.196 ± 0.036 for (20) Massalia, consistent with typical S-type asteroid values (for example, 0.258 ± 0.087 (ref. 43) and 0.208 ± 0.079 (ref. 44)). This refined albedo constrains the pre-atmospheric radius of the asteroid, based on brightness alone, to 35–55 cm (ref. 36).

Measurements of cosmogenic noble gases for five SPLV samples show a pronounced excess of ^{80}Kr and, less well resolved, of ^{82}Kr, which are probably due to neutron capture by ^{79}Br and ^{81}Br. Such neutron-induced isotopes are produced in greater depths when the secondary neutrons have slowed down to enable efficient capture, indicating that 2023 CX1 was at least 30 cm in radius[45].

By measuring the activities of short-lived radionuclides, such as ^{22}Na, ^{54}Mn, ^{57}Co and ^{60}Co (Supplementary Table 4), GS of SPLV samples further constrained the size of the meteoroid. The low abundance of ^{60}Co indicates that the meteoroid was too small to sustain a full nucleonic cascade within its interior[46]. The pre-atmospheric radius was estimated from the short-lived radionuclide concentrations combined with the bulk chemical composition of the meteorite (Supplementary Table 3) and Monte Carlo simulations[46–48]. The measured concentrations of ^{60}Co and ^{26}Al yielded radius estimates of 25 ± 4 cm and 28 ± 12 cm, respectively. The ^{26}Al activity in SPLV sample 1, measured using IAMS, indicated a minimum pre-atmospheric radius of 20 cm (Supplementary Table 5).

The atmospheric entry of 2023 CX1 generated an infrasound signal that was recorded by several arrays in Europe, North Africa and Russia. From the observed wave periods, the overall energy released during the event was $0.029^{+0.026}_{-0.014}$ kt of TNT equivalent ($1.2^{+1.1}_{-0.6} \times 10^{11}$ J; 'Infrasound analysis of the meteor'). This corresponds to an initial mass of $1{,}230^{+2{,}300}_{-630}$ kg and a radius of 36–55 cm, consistent with telescopic estimates.

Meteor optical analysis

The fireball trajectory and velocity were determined using the line-of-sight least-squares method[49,50]. Cameras from the Global Meteor Network (GMN) in the UK, where the skies were clear, captured the initial phase of the fireball. Absolute timing was obtained from the radiometer of a European Fireball Network camera in Tautenburg, Germany. Mobile phone recordings taken close to the end of the fireball, several of which were handheld, enabled a determination of the middle and end segments of the fireball. Photometry was done on one GMN camera, one mobile phone, one security camera and another low-sensitivity record from a mobile phone showing no stars but the Moon. In addition, the bright part was covered by one all-sky video recorded under an overcast sky and one calibrated luxmeter under an overcast sky (both in the UK) and the radiometer in Tautenburg, with a low signal-to-noise ratio but high temporal resolution.

The trajectory was computed using a least-squares fit to lines of sight[49] and independently verified with a Monte Carlo trajectory estimation approach[51]. No single straight-line trajectory solution could reproduce the motion of the meteoroid both before and after the main fragmentation event at 27–29 km altitude due to a measurable change in direction following the flare. Accurate determination of the trajectory therefore required fitting two separate solutions to the observations, one before and one after the fragmentation. The resulting trajectory parameters are summarized in Extended Data Table 3.

The light curve and deceleration of the main body and individual fragments were fitted by the semi-empirical fragmentation model of ref. 14. The same 4% luminous efficiency was used for both big and small fragments. The usually used values are 5% for big and 2.5% for small fragments[14]. The drag and shape coefficients were set to $\Gamma A = 0.7$ and the density was set to 3,300 kg m^{-3}.

For SPLV, an ablation coefficient σ of 0.003 kg MJ^{-1} was found to best reproduce the light curve before the flare, consistent with pure thermal ablation in the absence of fragmentation[52]. Owing to the limited observational coverage after the flare, the ablation coefficients of individual fragments could not be rigorously constrained. A standard value of 0.005 kg MJ^{-1} (ref. 14) was assumed for all fragments except one and was found to be consistent with the available data. The only exception was fragment A, whose dynamics required an elevated $\sigma = 0.015 \pm 0.003$ kg MJ^{-1} to adequately match the observed deceleration, indicating that there may have been further fragmentation along the trajectory. The dynamics of fragment A could alternatively be fitted using a standard $\sigma = 0.005$ kg MJ^{-1} combined with one or two fragmentation events, although the available observations do not allow for robust constraints on the timing and mass change associated with such events.

Strewn-field modelling

Independent modelling approaches were combined to analyse the meteorite strewn field. The landing positions of the nine individual fragments observed in video recordings were predicted using dark flight (DF) computations based on the ALADIN (Aire Limitée Adaptation dynamique Développement International) atmospheric wind model at 03:00 UTC. Meteorological wind models were provided without associated uncertainties. Other DF computations using alternative wind profiles (for example, radiosonde data from the Herstmonceux area) occasionally resulted in a slight overall shift in the strewn-field position but did not affect the modelled dispersion of the meteorites. For the main analysis, we used the wind model that provided the best agreement with the locations of the recovered meteorites.

To explain the concentration of meteorites recovered south-east of Angiens, we simulated the DF of hypothetical spherical fragments ranging from 1 g to 66 g released during the flare with various trajectory deviations. For each important fragmentation or dust release event, five representative fragments were modelled, one following the original trajectory and four deviating by up to 5° in the up, down, left and right directions. Each underwent ablation and DF simulation to determine its impact point (orange circles in Fig. 2). The limit 5° deviation was chosen to match the observed displacement of the most off-axis recovered meteorite (4), although it should be assumed that deviations follow a normal distribution with an outer edge around 5°. Although large, such deviations are plausible given the 0.8° offset measured for the most massive fragment (A) after the flare. This behaviour may reflect an explosive fragmentation process, possibly involving chemical reactions such as magnesium oxidation. Although simplified, this approach offers a useful approximation of how lateral dispersion may have shaped the final strewn field.

Other DF models were produced for fragments of different masses and shapes and released at various altitudes. First, a DF model was applied to small (<50 g) fragments ejected at the main flare, accounting for shape variations (conical, brick and spherical) to evaluate drag effects[28]. For SPLV, higher drag (for example, conical shapes) shifted the predicted strewn field north along the central line, although a lower drag (spherical shapes) shifted it south-east. A scenario using an intermediate shape (brick) is shown in Fig. 2 as a blue-shaded area. Another limiting case, assuming larger conical and spherical fragments released at the end of the visible path of the fireball, is illustrated in Fig. 2 as orange- and purple-shaded areas.

Infrasound analysis of the meteor

The atmospheric entry of 2023 CX1 generated an infrasound signal that was recorded by several stations of the Comprehensive Nuclear-Test-Ban Treaty Organization and by several arrays in the Netherlands (Royal Netherlands Meteorological Institute), the United Kingdom and France (French Alternative Energies and Atomic Energy Commission), including at a station located within 150 km from the fall in Flers, Normandy. For all International Monitoring System stations (with station labels starting with 'I' in Extended Data Table 4), the procedure for a bolide infrasound analysis described in refs. 53–55 was followed.

In this procedure, the best beam is formed at each array in time windows of 20-s duration near the time of the strongest bolide acoustic arrival. For SPLV fireball infrasound signals, a Butterworth filter band-pass of 0.6–7 Hz was found to maximize the signal-to-noise ratio of the acoustic signal. A cross-correlation of all infrasound array elements was then performed, and the apparent back azimuth and trace speed across the array computed in each time window based on the direction of the best beam. The bolide signal was defined across all time windows where the normalized cross-correction was above the background level, roughly 1 min in this instance. All array elements were then stacked using the best-beam direction, and a Hilbert transform was applied to estimate the amplitude envelope. Using the stacked waveform, the period at maximum amplitude was then measured by manually identifying the points where the waveforms cross the zero-amplitude axis for one wavelength centred at maximum amplitude.

The characteristics of the infrasound signals recorded by each station are detailed in Extended Data Table 4. To estimate the source energy, the empirical relation between multi-station period averages and yield given in ref. 54 was used (using the period at maximum amplitude zero crossing method in ref. 56 and the peak in the bolide infrasound signal power spectral density[54]). This multi-station period relation is of the form $E(\mathrm{kT}) = 10^{(3.28\log_{10}(P)+0.71)/1{,}000}$, where $E(\mathrm{kT})$ is the estimated source energy in kilotons TNT equivalent and P is the average period (in seconds) at maximum amplitude found through simple arithmetic averaging for all infrasound stations that detected the same bolide.

Seismo-acoustic analysis of the meteor

The seismo-acoustic wave was recorded by several seismic sensors in northern France and southern UK, which are part of the Réseau Sismologique et géodésique Français (French permanent broadband seismic network)[57] and the Great Britain Seismograph Network, respectively. The waves were also recorded by the Raspberry Pi Shake & Boom citizen science initiative, including four stations located within 150 km from the event (Extended Data Table 5 and Supplementary Fig. 1). Arrival times were evaluated using atmospheric models from the European Centre for Medium-Range Weather Forecasts (ECMWF IFS cycle 38r2), and three-dimensional (3D) ray-tracing simulations calculated with WASP-3D (ref. 58). One eigenray was identified for each arrival and celerity models were extracted by dividing the 3D distances in Cartesian coordinates by the travel times.

To account for the effects of unresolved gravity waves in the atmospheric models used[59] on the propagation, the errors of the predicted arrival times were estimated by adding 1,000 random perturbations uniformly distributed throughout ±10 m s^{-1} to the 3D celerity models. For each realization, a 3D location was found using a nonlinear least-squares solver[60] that optimizes the latitude, longitude, origin time and altitude of the fragmentation from the minimization of the root-mean-square time residuals. The best agreement between the theoretical and observed arrival times was reached for a source at latitude 49.81° ± 0.05° N, longitude 0.64° ± 0.07° E and a height of 27.9 ± 1.0 km, in agreement with the optical data (Extended Data Table 2).

Contributions of citizen science networks

Citizen contributions were crucial at every stage of the 2023 CX1 analysis. Shortly after its discovery, amateur astronomers worldwide performed numerous follow-up observations, which enabled the orbit of the asteroid to be refined. Timely social media communication led to a large-scale observational campaign targeting the fireball in the atmosphere. Still images and videos recorded using handheld phones (for example, from La Fresnaye) were essential for computing the trajectory of the bolide. Observers also recorded calibration images with their devices to aid computation of its trajectory. Several cameras of the GMN hosted by amateur astronomers caught the fireball. In addition to professional infrasound and seismic measurements, the citizen project Raspberry Pi & Boom network acquired and analysed seismic data, contributing to the analysis of the fragmentation of 2023 CX1. Finally, the rapid mobilization of the public in Normandy was crucial to the recovery of meteorites. Half of the meteorites collected through the FRIPON/Vigie-Ciel citizen science project were found by volunteers. All meteorites retrieved by the Vigie-Ciel team were collected responsibly and in accordance with local legislation.

Meteorite density

Overlapping images were taken from various angles to document the full exterior of four fragments of different sizes. Structure-from-motion photogrammetry was used to process these images and reconstruct 3D shape models using the software Agisoft Metashape Professional (v.2.0.2). In various steps that involve (1) camera-matching, the generation of (2) a sparse cloud, (3) a dense cloud and scale bars used during the photo-documentation procedure, the software is capable of rendering true-size 3D shape models. Other 3D models were also independently obtained through laser scanning. Estimates of the volumes of the generated 3D shape models were then determined with the software Meshlab (v.2022.02) and used with the mass of the fragment to find their bulk rock densities (Supplementary Table 6).

Mass spectrometry of the noble gases in the meteorite

Cosmogenic nuclides are produced by the irradiation of surface materials by primary cosmic-ray protons of both Galactic and solar origin. They serve as valuable tracers for investigating the origin and characteristics of meteorites, including the pre-atmospheric size of the meteoroid, CRE age and the shielding depth of individual fragments. To reconstruct the exposure history of 2023 CX1, we analysed noble gases for five SPLV meteorite fragments recovered across the strewn field.

All stable He–Xe isotopes were measured at ETH Zurich using the in-house-built noble gas mass spectrometer Albatros[61]. One aliquot each was measured from SPLV fragments 1, 4, 10, 13 and 26. The sample fragments (~16–23 mg; Extended Data Table 7) were wrapped in Al foil and preheated at ~110 °C in ultrahigh vacuum for several days before analysis to release adsorbed atmospheric gases. The noble gases were extracted by fusion in a Mo crucible at ~1,700 °C for ~25 min. A re-extraction at ~1,750 °C performed for SPLV 13 verified full gas extraction (gas amounts were <1% of that in the main step for all elements). Blank corrections were <0.3% of the signals for all He and Ne isotopes, <4.4% for ^{38}Ar and ^{40}Ar, <16% for ^{36}Ar and all Kr isotopes, and <3% for all Xe isotopes.

Noble gas measurements revealed that the He, Ne and Ar isotopic compositions of SPLV samples are mostly cosmogenic (Extended Data Table 6). No solar wind component was detected, indicating that SPLV is not a regolithic breccia. Radiogenic (rad) ^{4}He and ^{40}Ar were also identified, with a trace of trapped (tr) Ar. The elemental ratios of the heavy noble gases as well as the ^{130,131}Xe/^{132}Xe ratios did not reveal substantial air contribution, reflecting the fast recovery of SPLV. The ^{129}Xe/^{132}Xe ratios elevated over the chondritic Xe indicate minor amounts of short-lived radionuclide ^{129}I-derived ^{129}Xe in all samples, indicating the incorporation of ^{129}I into SPLV early in the Solar System (Extended Data Table 6).

The contribution from cosmogenic nuclides was derived as follows. All samples lack evidence for a trapped Ne component. Thus, He and Ne in all samples are purely cosmogenic, apart from ^{4}He (Extended Data Table 7). The ^{36}Ar/^{38}Ar ratios measured for all samples are slightly higher (~0.98–1.53) than typical cosmogenic values (0.63–0.67)[62], indicating the presence of minor Ar$_{\mathrm{tr}}$ in addition to dominant Ar$_{\mathrm{cos}}$ and ^{40}Ar$_{\mathrm{rad}}$. A two-component deconvolution was performed between typical $(^{36}\mathrm{Ar}/^{38}\mathrm{Ar})_{\mathrm{cos}}$ and $(^{36}\mathrm{Ar}/^{38}\mathrm{Ar})_{\mathrm{tr}}$ of 5.32–5.34 (covering *Q* and air compositions) to determine ^{38}Ar$_{\mathrm{cos}}$ (Extended Data Table 7) in these samples. $(^{80}\mathrm{Kr}/^{82}\mathrm{Kr})_{\mathrm{excess}}$ ratios were determined by assuming ^{86}Kr to be entirely trapped, $(^{80-83}\mathrm{Kr}/^{86}\mathrm{Kr})_{\mathrm{tr}}$ covering *Q* and air, and applying a typical $(^{80,82}\mathrm{Kr}/^{83}\mathrm{Kr})_{\mathrm{cos}}$ ratio for ordinary chondrites (0.487–0.585 over 0.705–0.771)[63]. We obtained $(^{80}\mathrm{Kr}/^{82}\mathrm{Kr})_{\mathrm{excess}}$ ratios (Extended Data Table 7) that are, within error, in a typical range expected for neutron-capture-derived Kr (ref. 64), confirming that the ^{80,82}Kr excesses are probably due to neutron capture by ^{79,81}Br.

The CRE age was determined as follows. We used the ordinary chondrite matrix model[47] and the bulk chemical composition of SPLV fragment 1 analysed by inductively coupled plasma – atomic emission spectrometry and inductively coupled plasma – mass spectrometry (Supplementary Table 3) to determine the production rates for cosmogenic ^{3}He, ^{21}Ne and ^{38}Ar and the respective CRE ages T_x for each sample. Each cosmogenic nuclide provided CRE ages that are similar for all samples analysed, except for a slightly higher T_{38} for fragment 10 and a smaller T_{38} for fragment 1. This small deviation was probably caused by target element heterogeneities (the so-called nugget effect) that predominantly influenced the ^{38}Ar$_{\mathrm{cos}}$ concentrations. We observed a tendency for lower CRE ages with lower mass of the respective cosmogenic isotope, that is, $T_3 < T_{21} \leq T_{38}$. This may indicate a loss of noble gases due to heating, for example, during atmospheric entry or passage close to the Sun, which preferentially affects the lighter noble gases. However, the SPLV data plot well on the correlation line in the Bern plot (Fig. 3 in ref. 65), indicating that there was no notable ^{3}He loss. Potentially, the deviations between various T_x could also result from slightly mismatching calculations for the production rates in the applied model. Lowering P_3 according to ref. 66, which reported differences between modelled and measured chondrite data, would bring the T_3 for SPLV into agreement with T_{21} and T_{38}. We consider the T_{21} ages most reliable, as ^{21}Ne$_{\mathrm{cos}}$ is less affected by heating and target element heterogeneities compared with cosmogenic ^{3}He and ^{38}Ar, respectively.

The ^{4}He$_{\mathrm{rad}}$ concentrations were calculated by using that ^{3}He is entirely cosmogenic, $(^{4}\mathrm{He}/^{3}\mathrm{He})_{\mathrm{cos}} = 5.2$–$6.1$ (ref. 62), and that ^{4}He$_{\mathrm{tr}}$ is negligible. The ^{40}Ar$_{\mathrm{rad}}$ concentrations were derived by determining ^{40}Ar$_{\mathrm{tr}}$ based on ^{36}Ar$_{\mathrm{tr}}$ (see deconvolution above) and $(^{40}\mathrm{Ar}/^{36}\mathrm{Ar})_{\mathrm{tr}} = 0$–$295.5$ (conservatively covering *Q*, with no trapped ^{40}Ar, and air composition). The slightly lower T_4 age of SPLV fragment 4 might be explained by variations in the phosphate (apatite and merrillite) abundance (~0.5–0.7% in L chondrites[67]) across the different SPLV fragments, as this mainly controls the U concentration in the material.

Gamma spectrometry

Fragments 2, 4 and 10 were also analysed for cosmogenic radionuclides using non-destructive GS at the low-background laboratory of Comenius University in Bratislava. This GS analysis provided an independent constraint on the pre-atmospheric radius of the impactor and the shielding depths of the meteorites, as well as a complementary estimate of the CRE age of 2023 CX1.

Two high-purity germanium detectors (Princeton Gamma Tech) and (Canberra/Mirion) of 70% and of 50% relative efficiency (for 1,332.5-keV gamma-rays from ^{60}Co), respectively, placed in low-background shields in the basement of the three-storey building were used for analyses. A detailed description of the gamma-ray spectrometers, measuring procedures, efficiency of the Monte Carlo detector, self-absorption and corrections for summation effects are given in refs. 68,69. The uncertainties in the results were mainly due to counting statistics, which were typically below 10%. The measuring time was from 30 days to 50 days, depending on the mass of the samples analysed. All measurements were corrected back to the date of the meteorite fall on 13 February 2023. Regular analyses using International Atomic Energy Agency and National Institute of Standards and Technology reference materials and participation in intercomparison exercises guarantee that results remain at a good quality.

The T_{26} CRE ages presented in Extended Data Table 7 were estimated using the ^{26}Al–^{21}Ne isotope pair method[20,70], based on the ^{21}Ne measurements in the same table. We found that the T_{26} ages are consistent with estimates obtained from single noble gas isotope methods, particularly with those derived from the ^{21}Ne method (Extended Data Table 7).

Instrumental accelerator mass spectrometry

Fragments 1, 4, 10, 13 and 26 were analysed using accelerator mass spectrometry at the Vienna Environmental Research Accelerator (VERA). Measurements of long-lived cosmogenic radionuclides in the SPLV samples provide key constraints on the pre-atmospheric size of the meteoroid and the shielding depths of the recovered fragments, thus offering valuable insights into the distribution of material during atmospheric fragmentation.

A distinctive innovation of VERA is an ion–laser interaction mass spectrometry system that enables isobar suppression by up to 14 orders of magnitude[71]. Consequently, the combination of ion–laser interaction mass spectrometry and accelerator mass spectrometry, so-called IAMS, allowed the direct detection of ^{26}Al/^{27}Al and ^{41}Ca/^{40}Ca in crushed SPLV samples containing ~1% intrinsic Al and Ca. The presence of isobars from the natively abundant elements (15% Mg and ~0.1% K) did not present any analytical issues, thereby rendering radiochemical separation unnecessary.

IAMS was conducted on small aliquots of homogenized powders of ~1 g of specimen 1, which was also used to determine the bulk chemistry (Supplementary Table 3), 245 mg of specimen 4, 233 mg of specimen 10, 226 mg of specimen 13 and 214 mg of specimen 26. To extract AlO$^-$ and measure ^{26}Al/^{27}Al (ref. 72), ~5 mg of the fine-grained powder was pressed into Cu cathodes without the use of a metal binder. To increase CaF_3^- extraction from the Cs ion sputter source, 0.9–1.4 mg of each SPLV powder sample was mixed with a factor of 9 by weight of PbF$_2$. This mixture was then pressed into Cu cathodes. In-house standards Dhurmsala (^{26}Al/^{27}Al = (1.287 ± 0.034) × 10^{-10}) and SMD-Ca-11 (^{41}Ca/^{40}Ca = (0.9944 ± 0.0092) × 10^{-11}), which are traceable to primary standards[73], were used for normalization.

To convert nuclide ratios into massic activities in disintegrations per minute per kilogram (Supplementary Table 5), the Al and Ca concentrations in Supplementary Table 3 (1.19% Al and 1.19% Ca) were used. These massic activities measured by IAMS were compared with Monte Carlo calculation-based radius- and depth-dependent production rates for ^{26}Al (ref. 48) and ^{41}Ca (ref. 47). The theoretical production rates are generally based on L-chondrite parameters and were adjusted to the bulk composition of SPLV in Supplementary Table 3, an oxygen content of 38.47% and the sulfur value of 2.22% from ref. 74. Oxygen, carbon (0.08%)[75] and nitrogen (1 μg g^{-1})[76] do not produce any ^{26}Al or ^{41}Ca, but in this way, all input elements including all relevant minor elements determined add up to 100%.

IAMS-determined nuclide ratios can be explained by sufficiently long CRE ages (Extended Data Table 7), resulting in saturation of ^{26}Al and ^{41}Ca in the samples. The reported ^{26}Al data have total 1σ uncertainties of 3.1–4.0%, which include counting statistics, sample scatter, variability in standard measurements (0.85%) and the nominal reference value uncertainty, all combined quadratically. The uncertainty in massic activity in terms of disintegrations per minute per kilogram also incorporates a 5% uncertainty for stable ^{27}Al, making it the largest contributor. Similarly, the ^{41}Ca/^{40}Ca data have 1σ uncertainties of 14–22%, accounting for counting statistics, sample scatter, variability in standard measurements and the nominal reference value uncertainty. For massic activity (in disintegrations per minute per kilogram), the extra 5% uncertainty for stable Ca (1.19%) contributed minimally.

Measurements of ^{26}Al concentrations using IAMS (Supplementary Table 5) show a discrepancy compared with values obtained by GS (Supplementary Table 4) across all measured SPLV samples. The lower ^{26}Al concentrations reported by IAMS indicate shallower shielding depths (ranging from 2.5 to 30 cm) than those previously estimated. Although the cause of this discrepancy remains under investigation, both IAMS and GS data confirm the absence of any correlation between shielding depth and sample position within the strewn field.

To our knowledge, the IAMS-measured ^{41}Ca/^{40}Ca ratios for the five SPLV samples represent one of the few ^{41}Ca depth profiles obtained for meteorites. They are especially rare for ordinary chondrites. The variations in these ratios are relatively narrow, ranging from 2.6 to 4.0 × 10^{-12}. When comparing these ratios with experimental depth-dependent IAMS ^{41}Ca/^{40}Ca data from the L5 chondrite Knyahinya (S.M. personal communication, 12 December 2024; shielding positions and radius of 45 cm from ref. 77), shallow shielding depths (<20 cm) can be constrained. However, no further conclusions on the radius or shielding depths of the SPLV samples can, at present, be drawn from the comparison with production rates from Monte Carlo simulations (for example, as noted by ref. 78).

Asteroid dynamical analysis

The orbital stability of 2023 CX1 was analysed through backwards integration of its nominal orbit and 99 clones generated from the orbital solution and covariance matrix of solution 14 in Table 1. Using a RADAU 15 integrator with a tolerance of 10^{-12} and a 1-day external time step, we considered the gravitational influences of the Sun, the eight planets and the Moon, based on the DE405 Planetary ephemeris[79].

Additionally, we used the METEOMOD orbital distribution model for meteoroids[21,22] to estimate the probability that 2023 CX1 originated from one of the asteroid families located between 1.9 au and 3.5 au. Probability distribution maps in near-Earth object space (semimajor axis and inclination) were employed to identify the source region of L-chondrite orbits (Extended Data Fig. 3). The probability of originating from a source was computed by normalizing and multiplying each map by the corresponding population of near-Earth objects (>1 m) in the near-Earth region. Results for the SPLV and Novo Mesto meteorites are provided in Supplementary Table 7. The Massalia$_2$ family produces low-inclination orbits compatible with the pre-atmospheric trajectories of the SPLV and Novo Mesto meteorites. This method differs from those used in previous models (for example, refs. 80,81), where sources correspond to resonances (for example, ν_6, 3:1, 5:2 or 2:1), thereby losing much of the information about the original orbital elements (a, e and i). In addition, METEOMOD uses the size versus frequency distributions of the sources, which serve as weights, and incorporate the taxonomy of the sources to prevent ambiguities.

Blast-wave pressure calculations

The propagation of the blast wave to the ground was simulated using the ALE3D hydrocode on the Aitken Supercomputer at NASA Ames.

Energy was deposited according to the meteor light-curve profiles for an adopted entry speed of 14 km s^{-1} and a total energy of 18 Mt. A constant luminous efficiency was assumed, so the energy deposition rate dE/dt was proportional to the luminosity. A domain was filled with ideal gas air using an isothermal atmosphere at 255 K and a scale height of 7.5 km. Simulation cells were aligned with the trajectory at 49.1°, and energy was deposited uniformly during the time the meteor was passing through each cell. For a larger meteor, there may also be an important amount of momentum imparted, but that was neglected in these simulations.

To efficiently propagate the blast wave to the ground, the energy deposition was scaled up to 18.4 Mt, producing a blast wave kilometres in length and allowing a much coarser mesh. Although this energy represents approximately one million times the kinetic energy of 2023 CX1, the distribution of the overpressure on the ground was expected to be like that of 2023 CX1, although at lower pressures. A real 18-Mt impactor would burst lower in the atmosphere than the energy profile simulated here. At the actual energy of 2023 CX1, the resulting shock waves would have a lower overpressure and be narrower but would still originate from the same points along the trajectory. Pressure waves travel faster at higher overpressures, but even in the 18-Mt case, they drop to near sonic speeds within a few kilometres of the source. This means that the pressure waves from a 2023 CX1-like event will combine in a similar pattern to those of the 18-Mt case, resulting in a comparable ground footprint but at non-damaging overpressure levels probably within background noise.

Data availability

Updated astrometric measurements of asteroid 2023 CX1 before impact are publicly available at the MPC (available at https://minorplanetcenter.net). The updated orbital solution is accessible via the JPL Small-Body Database Browser (https://ssd.jpl.nasa.gov/tools/sbdb_lookup.html#/?sstr=2023). Data supporting the fireball trajectory, photometry, strewn field computations and seismo-acoustic analysis are provided in ref. 82.

Code availability

The proprietary software used in this analysis includes methods for computing the orbit of the asteroid, analysing the fragmentation of the fireball, modelling the strewn field and simulating propagation of the blast wave using ALE3D (https://sd.llnl.gov/stockpile-science/high-performance-computing/proprietary-software). Some of the optical fireball data were calibrated using the open-source SkyFit2 software, which is part of the RMS library available at https://github.com/CroatianMeteorNetwork/RMS. The trajectory parameters for the fireball were independently confirmed using WesternMeteorPyLib (wmpl), which was also used to compute the trajectory and support the modelling of the strewn field. That software is available at https://github.com/wmpg/WesternMeteorPyLib. Probabilities of originating from the Massalia asteroid family were computed using the METEOMOD model, accessible at https://sirrah.troja.mff.cuni.cz/~mira/meteomod/meteomod.php.

References

1. Brown, P. G. et al. A 500-kiloton airburst over Chelyabinsk and an enhanced hazard from small impactors. *Nature* **503**, 238–241 (2013).
2. Greenwood, R. C., Burbine, T. H. & Franchi, I. A. Linking asteroids and meteorites to the primordial planetesimal population. *Geochim. Cosmochim. Acta* **277**, 377–406 (2020).
3. Sárneczky, K. 2023 CX1. *Minor Planet Electron. Circ.* **2024-C103**, 1 (2024).
4. Colas, F. et al. The FRIPON and Vigie-Ciel networks. In *Proc. International Meteor Conference* (eds Rault, J.-L. & Roggemans, P.) 34–38 (International Meteor Organization, 2014).
5. Colas, F. et al. FRIPON: a worldwide network to track incoming meteoroids. *Astron. Astrophys.* **644**, A53 (2020).
6. Jenniskens, P. & Colas, F. 2023 CX1. *Cent. Bur. Electron. Telegr.* **5221**, 1 (2023).
7. Zanda, B. et al. Recovery and planned study of the Saint-Pierre-le-Viger meteorite: an achievement of the FRIPON/Vigie-Ciel citizen science program. *LPI Contrib.* **2990**, 6206 (2023).
8. Gattacceca, J. et al. The Meteoritical Bulletin, No. 112. *Meteorit. Planet. Sci.* **59**, 1820–1823 (2024).
9. Bischoff, A. et al. Saint-Pierre-le-Viger (L5–6) from asteroid 2023 CX1 recovered in Normandy, France—220 years after the historic fall of L'Aigle (L6 breccia) in the neighborhood. *Meteorit. Planet. Sci.* **58**, 1385–1398 (2023).
10. Devogèle, M. et al. Aperture photometry on asteroid trails: detection of the fastest rotating near-Earth object. *Astron. Astrophys.* **689**, A63 (2024).
11. Popova, O., Borovička, J. & Campbell-Brown, M. D. in *Meteoroids: Sources of Meteors on Earth and Beyond* (eds Ryabova, G. O. et al.) 9 (Cambridge Univ. Press, 2019).
12. Fadeenko, Y. I. Destruction of meteoroids in the atmosphere. *Combust. Explos. Shock Waves* **3**, 172–174 (1967).
13. Popova, O. et al. Very low strengths of interplanetary meteoroids and small asteroids. *Meteorit. Planet. Sci.* **46**, 1525–1550 (2011).
14. Borovička, J., Spurný, P. & Shrbený, L. Two strengths of ordinary chondritic meteoroids as derived from their atmospheric fragmentation modeling. *Astron. J.* **160**, 42 (2020).
15. Jenniskens, P. et al. Bolide fragmentation: what parts of asteroid 2008 TC3 survived to the ground? *Meteorit. Planet. Sci.* **57**, 1641–1664 (2022).
16. Whipple, A. L. Lyapunov times of the inner asteroids. *Icarus* **115**, 347–353 (1995).
17. Swindle, T. D., Kring, D. A. & Weirich, J. R. in *Advances in* ^{40}*Ar/*^{39}*Ar Dating: From Archaeology to Planetary Sciences* (eds Jourdan, F. et al.) 333–347 (Geological Society, 2014).
18. Herzog, G. F. & Caffee, M. W. in *Meteorites and Cosmochemical Processes* (ed. Davis, A. M.) 419–454 (Elsevier, 2014).
19. Brown, P. G. et al. The Golden meteorite fall: fireball trajectory, orbit, and meteorite characterization. *Meteorit. Planet. Sci.* **58**, 1773–1807 (2023).
20. Povinec, P. P. et al. Radionuclides in Chassigny and Nakhla meteorites of Mars origin: implications for their pre-atmospheric sizes and cosmic-ray exposure ages. *Planet. Space Sci.* **186**, 104914 (2020).
21. Brož, M. et al. Young asteroid families as the primary source of meteorites. *Nature* **634**, 566–571 (2024).
22. Marsset, M. et al. The Massalia asteroid family as the origin of ordinary L chondrites. *Nature* **634**, 561–565 (2024).
23. Ceplecha, Z., Spurný, P., Borovička, J. & Keclikova, J. Atmospheric fragmentation of meteoroids. *Astron. Astrophys.* **279**, 615–626 (1993).
24. Borovička, J. & Spurný, P. The Carancas meteorite impact-encounter with a monolithic meteoroid. *Astron. Astrophys.* **485**, L1–L4 (2008).
25. Brown, P. et al. Analysis of a crater-forming meteorite impact in Peru. *J. Geophys. Res.: Planets* **113**, E09007 (2008).
26. Borovička, J., Spurný, P., Grigore, V. I. & Svoreň, J. The January 7, 2015, superbolide over Romania and structural diversity of meter-sized asteroids. *Planet. Space Sci.* **143**, 147–158 (2017).
27. Vida, D. et al. Novo Mesto meteorite fall—trajectory, orbit, and fragmentation analysis from optical observations. In *Proc. Europlanet Science Congress 2021* https://doi.org/10.5194/epsc2021-139 (Copernicus Meetings, 2021).

28. Vida, D. et al. Accurate characterization of metre-sized impactors through casual bolide observations—Novo Mesto superbolide as evidence for a new class of high-risk objects. In *Proc. 8th IAA Planetary Defense Conference* (International Academy of Astronautics, 2023).
29. Jenniskens, P. et al. Orbit and origin of the LL7 chondrite Dishchii'bikoh (Arizona). *Meteorit. Planet. Sci.* **55**, 535–557 (2020).
30. Morrison, D. *Tunguska Workshop: Applying Modern Tools to Understand the 1908 Tunguska Impact*. Technical Memorandum NASA/TM–220174 (NASA, 2018).
31. Trigo-Rodríguez, J. M. et al. A numerical approach to study ablation of large bolides: application to Chelyabinsk. *Adv. Astron.* **2021**, 8852772 (2021).
32. Moskovitz, N. A. et al. A common origin for dynamically associated near-Earth asteroid pairs. *Icarus* **333**, 165–176 (2019).
33. Mommert, M. PHOTOMETRYPIPELINE: an automated pipeline for calibrated photometry. *Astron. Comput.* **18**, 47–53 (2017).
34. Gaia Collaboration. Gaia Data Release 2: summary of the contents and survey properties. *Astron. Astrophys.* **616**, A1 (2018).
35. Flewelling, H. A. et al. The Pan-STARRS1 database and data products. *Astrophys. J. Suppl. Ser.* **251**, 7 (2020).
36. Bowell, E. et al. in *Asteroids II* (eds Binzel, R. P. et al.) 524–556 (Univ. Arizona Press, 1989).
37. Pál, A. FITSH: a software package for image processing. *Mon. Not. R. Astron. Soc.* **421**, 1825–1837 (2012).
38. Colomé, J. et al. The OAdM robotic observatory. *Adv. Astron.* **2010**, 183016 (2010).
39. Raab, H. Astrometrica: astrometric data reduction of CCD images. *Astrophys. Source Code Library* ascl:1230.012 (2012).
40. Gaffey, M. J. et al. Mineralogical variations within the S-type asteroid class. *Icarus* **106**, 573–602 (1993).
41. Nakamura, T. et al. Itokawa dust particles: a direct link between S-type asteroids and ordinary chondrites. *Science* **333**, 1113 (2011).
42. Berthier, J., Carry, B., Mahlke, M. & Normand, J. SsODNet: Solar System Open Database Network. *Astron. Astrophys.* **671**, A151 (2023).
43. DeMeo, F. E. & Carry, B. The taxonomic distribution of asteroids from multi-filter all-sky photometric surveys. *Icarus* **226**, 723–741 (2013).
44. Usui, F. et al. Albedo properties of main belt asteroids based on the all-sky survey of the infrared astronomical satellite AKARI. *Astrophys. J.* **762**, 56 (2013).
45. Eberhardt, P., Geiss, J. & Lutz, H. Neutrons in meteorites. *Earth Sci. Meteorit.* **34**, 143–168 (1963).
46. Wieler, R. et al. Exposure history of the Torino meteorite. *Meteorit. Planet. Sci.* **31**, 265–272 (1996).
47. Leya, I. & Masarik, J. Cosmogenic nuclides in stony meteorites revisited. *Meteorit. Planet. Sci.* **44**, 1061–1086 (2009).
48. Leya, I., Hirtz, J. & David, J.-C. Galactic cosmic rays, cosmic-ray variations, and cosmogenic nuclides in meteorites. *Astrophys. J.* **910**, 136 (2021).
49. Borovička, J. The comparison of two methods of determining meteor trajectories from photographs. *Bull. Astron. Inst. Czechoslov.* **41**, 391 (1990).
50. Borovička, J. et al. Data on 824 fireballs observed by the digital cameras of the European Fireball Network in 2017-2018. I. Description of the network, data reduction procedures, and the catalog. *Astron. Astrophys.* **667**, A97 (2022).
51. Vida, D., Gural, P. S., Brown, P. G., Campbell-Brown, M. & Wiegert, P. Estimating trajectories of meteors: an observational Monte Carlo approach. I. Theory. *Mon. Not. R. Astron. Soc.* **491**, 2688–2705 (2019).
52. Ceplecha, Z. & Revelle, D. O. Fragmentation model of meteoroid motion, mass loss, and radiation in the atmosphere. *Meteorit. Planet. Sci.* **40**, 35 (2005).
53. Edwards, W. N., Brown, P. G. & ReVelle, D. O. Estimates of meteoroid kinetic energies from observations of infrasonic airwaves. *J. Atmos. Sol.-Terr. Phys.* **68**, 1136–1160 (2006).
54. Ens, T. A., Brown, P. G., Edwards, W. N. & Silber, E. Infrasound production by bolides: a global statistical study. *J. Atmos. Sol.-Terr. Phys.* **80**, 208–229 (2012).
55. Gi, N. & Brown, P. G. Refinement of bolide characteristics from infrasound measurements. *Planet. Space Sci.* **143**, 169–181 (2017).
56. ReVelle, D. O. Historical detection of atmospheric impacts by large bolides using acoustic-gravity waves. *Ann. NY Acad. Sci.* **822**, 284–302 (1997).
57. RESIF-RLBP French Broad-band network, RESIF-RAP strong motion network and other seismic stations in metropolitan France. *RESIF Information System* https://doi.org/10.15778/RESIF.FR (1995).
58. Virieux, J., Garnier, N., Blanc, E. & Dessa, J.-X. Paraxial ray tracing for atmospheric wave propagation. *Geophys. Res. Lett.* **31**, L20106 (2004).
59. Listowski, C. et al. Stratospheric gravity waves impact on infrasound transmission losses across the International Monitoring System. *Pure Appl. Geophys.* **181**, 33 (2024).
60. Moré, J. J. in *Numerical Analysis* (ed. Watson, G. A.) 105–116 (Springer, 2006).
61. Riebe, M. E. I. et al. Cosmic-ray exposure ages of six chondritic Almahata Sitta fragments. *Meteorit. Planet. Sci.* **52**, 2353–2374 (2017).
62. Wieler, R. Cosmic-ray-produced noble gases in meteorites. *Rev. Mineral. Geochem.* **47**, 125–170 (2002).
63. Leya, I. et al. Calibration of cosmogenic noble gas production based on ^{36}Cl-^{36}Ar ages. Part 2. The ^{81}Kr-Kr dating technique. *Meteorit. Planet. Sci.* **50**, 1863–1879 (2015).
64. Martin, I. H. M. J. A=71. Zn, Ga, Ge, As, Se, Br, Kr. *Nucl. Data Sheets Sect. B* **1**, 13–26 (1966).
65. Nishiizumi, K., Regnier, S. & Marti, K. Cosmic ray exposure ages of chondrites, pre-irradiation and constancy of cosmic ray flux in the past. *Earth Planet. Sci. Lett.* **50**, 156–170 (1980).
66. Dalcher, N. et al. Calibration of cosmogenic noble gas production in ordinary chondrites based on ^{36}Cl-^{36}Ar ages. Part 1. Refined production rates for cosmogenic ^{21}Ne and ^{38}Ar. *Meteorit. Planet. Sci.* **48**, 1841–1862 (2013).
67. Lewis, J. A. & Jones, R. H. Phosphate and feldspar mineralogy of equilibrated L chondrites: the record of metasomatism during metamorphism in ordinary chondrite parent bodies. *Meteorit. Planet. Sci.* **51**, 1886–1913 (2016).
68. Povinec, P., Sýkora, I., Ferrière, L. & Koeberl, C. Analyses of radionuclides in the Oued Awlitis 001 and Galb Inal lunar meteorites by HPGe gamma-ray spectrometry. *J. Radioanal. Nucl. Chem.* **324**, 349–357 (2020).
69. Kováčik, A., Sýkora, I. & Povinec, P. P. Monte Carlo and experimental efficiency calibration of gamma-spectrometers for non-destructive analysis of large volume samples of irregular shapes. *J. Radioanal. Nucl. Chem.* **298**, 665–672 (2013).
70. Eugster, O., Busemann, H., Lorenzetti, S. & Terribilini, D. Ejection ages from krypton-81-krypton-83 dating and pre-atmospheric sizes of Martian meteorites. *Meteorit. Planet. Sci.* **37**, 1345–1360 (2002).
71. Martschini, M. et al. 5 years of ion-laser interaction mass spectrometry—status and prospects of isobar suppression in IAMS by lasers. *Radiocarbon* **64**, 555–568 (2022).
72. Lachner, J. et al. Highly sensitive 26Al measurements by ion-laser-interaction mass spectrometry. *Int. J. Mass Spectrom.* **465**, 116576 (2021).
73. Rugel, G. et al. The first four years of the AMS-facility DREAMS: status and developments for more accurate radionuclide data. *Nucl. Instrum. Methods Phys. Res. Sect. B* **370**, 94–100 (2016).

74. Cripe, J. D. & Moore, C. B. Total sulfur content of ordinary chondrites. *Meteoritics* **10**, 387 (1975).
75. Grady, M. M., Wright, I. P. & Pillinger, C. T. A preliminary investigation into the nature of carbonaceous material in ordinary chondrites. *Meteoritics* **24**, 147 (1989).
76. Hashizume, K. & Sugiura, N. Nitrogen isotopes in bulk ordinary chondrites. *Geochim. Cosmochim. Acta* **59**, 4057–4069 (1995).
77. Graf, T. et al. Cosmogenic nuclides and nuclear tracks in the chondrite Knyahinya. *Geochim. Cosmochim. Acta* **54**, 2511–2520 (1990).
78. Bischoff, A. et al. The anomalous polymict ordinary chondrite breccia of Elmshorn (H3-6)—late reaccretion after collision between two ordinary chondrite parent bodies, complete disruption, and mixing possibly about 2.8 Gyr ago. *Meteorit. Planet. Sci.* **59**, 2321–2356 (2024).
79. Standish, E. M. *JPL Planetary and Lunar Ephemerides*. Interoffice Memo DE405/LE405 (JPL, 1998).
80. Granvik, M. et al. Debiased orbit and absolute-magnitude distributions for near-Earth objects. *Icarus* **312**, 181–207 (2018).
81. Nesvorný, D. et al. NEOMOD: a new orbital distribution model for near-Earth objects. *Astron. J.* **166**, 77 (2023).
82. Egal, A. et al. 2023 CX1 - Saint-Pierre-le-Viger data. *Zenodo* https://doi.org/10.5281/zenodo.15328378 (2025).

Acknowledgements

We thank M. Alexandersen (MPC) for reviewing and correcting station coordinates in the MPC database. Model wind data was provided by R. Brožková from the Czech Hydrometeorological Institute. Data visualization was provided by P. Geoffroy. We thank E. J. Christensen, R. L. Seaman and J. Stone for providing observations from the Catalina Sky Survey. The following camera operators contributed 2023 CX1 imaging to the FRIPON, GMN and UKMON networks: M. Rushton, A. Pratt, S. Saunders, J. Olver, N. Russel and M. McIntyre. Targeted fireball observations were made by V. Devillepoix, J.-L. Devillepoix, P. Devillepoix, A. Favre, A. Greenway, L. Greenway, Y. Trotel and P. Wright, among others. Observatori del Montsec-IEEC recorded the fireball from Sant Esteve de la Farga, Lleida, Catalonia, at a nominal distance of 900 km. We thank B. Gladman for the dynamical computations of the escape route of the asteroid. We thank F. Nikodem, L. Smuła and M. Smuła for providing the coordinates and masses of the fragments found. We thank R. Wieler for contributing to the discussion of the noble gas results. The help of the VERA cosmogenics team, especially S. Adler, R. Golser, P. Steier and C. Vivo-Vilches, is highly appreciated. The meteorite field search was supported by members of the FRIPON/Vigie-Ciel citizen science network, with participants listed at https://www.vigie-ciel.org/2024/10/21/2023cx1-splv-consortium. A.E., D.V., P. Brown and P.W. were supported in part by the NASA Meteoroid Environment Office (Cooperative Agreement 80NSSC21M0073). J.B. and P. Spurný were supported by the Czech Science Foundation (Grant No. 19-26232X). S.A. received funding from the European Union's Horizon Europe research and innovation programme (Marie Skodowska-Curie Grant Agreement No. 101150536) for the project FLAME. D.F. and S.N. conducted their research at the Jet Propulsion Laboratory, California Institute of Technology, under a contract with NASA (80NM0018D0004). The Czech Science Foundation supported this research (Grant Nos. 25-16507S to M. Birlan and 25-16789S to J. Hanuš). Funding was also received from the Hungarian National Research, Development, and Innovation Office (Grant Nos. K-138962 and GINOP-2.3.2-15-2016-00003) and from the Slovak Science and Grant Agency (Project VEGA-1/0487/23 to P.P., I.S. and I.K.). D. Krietsch, L.M.E. and H.B. were supported by the Swiss SNF and NCCR PlanetS (Grant Nos. 51NF40_205606 and SNF_219860). The VERA cosmogenics team was supported by the ChETEC-INFRA (Horizon 2020, Grant No. 101008324). T.S.-R. acknowledges funding from Ministerio de Ciencia e Innovación (Spanish Government; Grant Nos. PGC2021 and PID2021-125883NB-C21). This work was (partially) supported by the Spanish MICIN/AEI/10.13039/501100011033 and by ERDF A way of making Europe by the European Union (Grant No. PID2021-122842OB-C21) and the Institute of Cosmos Sciences, University of Barcelona (Unidad de Excelencia María de Maeztu; Grant No. CEX2019-000918-M). J.M.T.-R. acknowledges support from the Spanish project funded by MCIN/AEI (Project PID2021-128062NB-I00). A.J. acknowledges support from the ANID Millennium Science Initiative (Grant Nos. ICN12_009 and IM23-0001). R.A.M. acknowledges support from FONDECYT/ANID (Grant No. 124 0049) and from ANID, Fondo GEMINI, Astrónomo de Soporte GEMINI-ANID (Grant No. 3223 AS0002). D.H. and J.J. were supported in part by the SIAA Foundation Interactive Astronomy and Astrophysics in Tübingen, Germany. The Joan Oró Telescope at the Montsec Observatory is owned by the Catalan Government and operated by the Institute of Space Studies of Catalonia (IEEC). The UK Fireball Alliance meteor camera observatory was supported by the Science and Technology Facilities Council (Grant No. ST/Y004817/1). P.J. was supported by NASA (Grant No. 80NSSC18K0854).

Author contributions

A.E., D.V., F.C. and B.Z. coordinated the research. A.E., D.V., B.Z. and P.J. drafted the paper. M. Micheli, K.S., A.P., D.F., S.N., L.C., F.O., D.H., J.J., P.D., T.S.-R. and A.E. collected and calibrated the data associated with asteroid discovery, imaging and astrometry. N.M., T.K., T.S.-R., J. Hanuš, M.D., L.B., K.K., M. Birlan, D.A.N., A. Sonka and F.L. collected and calibrated the data related to the asteroid photometry. P.W., P.V., M. Marsset, M. Brož, P. Shober, A.L. and A.E. completed the asteroid dynamical analysis. J.B., P. Spurný, D.V., H.A.R.D., A.E., S.A., R.N., M. McIntyre, D.Š., J. Vaubaillon, K.B., J.D. and the FRIPON International Team (FIT) collected and analysed the data relevant to meteor triangulation and photometry. J.B., P. Spurný, D.V. and H.A.R.D. undertook the fragmentation and strewn-field calculation. F.C., S. Bouley, A. Steinhausser, B.Z., P.V., J. Vaubaillon, A.M., K.A., L.M., J.D., K.B., M. Birlan, S. Bouquillon, S.J., P. Beck, P.J. and FIT collected and calibrated the data associated with meteorite recovery and search campaign coordination. P. Brown, J.A. and L.E. collected and calibrated the data for the infrasound analysis. A.L.P., G.M.-R., J. Vergoz, J. Vergne and L.McF. collected and calibrated the data related to the seismo-acoustic analysis. B.Z., J.G., L.F., M.G., S.P., I.B., J.-A.B. and P.S.-J. collected and calibrated the data relevant to meteorite sampling and characterization. D. Krietsch, H.B., C.M. and L.M.E. collected and calibrated the data in the analysis of noble gas isotopes in the meteorites. P.P., I.S., I.K., O.M., M. Martschini, S.M. and A.W. collected and calibrated the data in the analysis of cosmogenic nuclides in the meteorites. S.d.V. collected and calibrated the data in the analysis of meteorite density. D.R. undertook the blast-wave pressure calculations. P.J., O.H. and P. Brown provided general guidance and improvements to the paper. All authors reviewed the results and approved the final version of the paper.

Competing interests

The authors declare no competing interests.

Additional information

Extended data is available for this paper at https://doi.org/10.1038/s41550-025-02659-8.

Supplementary information The online version contains supplementary material available at https://doi.org/10.1038/s41550-025-02659-8.

Correspondence and requests for materials should be addressed to Auriane Egal.

Peer review information *Nature Astronomy* thanks Thomas Burbine, Toshihiro Kasuga and Eleanor Sansom for their contribution to the peer review of this work.

Reprints and permissions information is available at www.nature.com/reprints.

Auriane Egal[1,2,3] ✉, Denis Vida[3], François Colas[1], Brigitte Zanda[1,4], Sylvain Bouley[1,5], Asma Steinhausser[1,6], Pierre Vernazza[1,7], Ludovic Ferrière[8,9], Jérôme Gattacceca[10], Mirel Birlan[1,11], Jérémie Vaubaillon[1], Karl Antier[12], Simon Anghel[1,11], Josselin Desmars[1,13], Kévin Baillié[1], Lucie Maquet[1], Sébastien Bouquillon[1], Adrien Malgoyre[14], Simon Jeanne[1], FRIPON International Team*, Jiří Borovička[15], Pavel Spurný[15], Hadrien A. R. Devillepoix[16], Marco Micheli[17], Davide Farnocchia[18], Shantanu Naidu[18], Peter Brown[3], Paul Wiegert[3], Krisztián Sárneczky[19], András Pál[20], Nick Moskovitz[21], Theodore Kareta[21], Toni Santana-Ros[22,23], Alexis Le Pichon[24], Gilles Mazet-Roux[24], Julien Vergoz[24], Luke McFadden[3], Jelle Assink[25], Läslo Evers[25,26], Daniela Krietsch[27], Henner Busemann[27], Colin Maden[27], Lisa Maria Eckart[27], Jean-Alix Barrat[28,29], Pavel Povinec[30], Ivan Sýkora[30], Ivan Kontul'[30], Oscar Marchhart[31], Martin Martschini[31], Silke Merchel[31], Alexander Wieser[31], Matthieu Gounelle[4], Sylvain Pont[4], Pierre Sans-Jofre[4], Sebastiaan de Vet[32,33], Ioannis Baziotis[34], Miroslav Brož[35], Michaël Marsset[36], Jérôme Vergne[37], Josef Hanuš[35], Maxime Devogèle[17], Luca Conversi[17], Francisco Ocaña[17], Luca Buzzi[38], Dan Alin Nedelcu[11], Adrian Sonka[11], Florent Losse[39], Philippe Dupouy[40], Korado Korlević[41], Dieter Husar[42], Jost Jahn[42], Damir Šegon[43], Mark McIntyre[44], Ralf Neubert[45], Pierre Beck[46], Patrick Shober[1,16], Anthony Lagain[10], Olivier Hernandez[2], Darrel Robertson[47] & Peter Jenniskens[48]

[1]FRIPON, LTE, Observatoire de Paris, PSL Research University, Sorbonne Université, CNRS, Université Lille, Paris, France. [2]Planétarium de Montréal, Espace pour la Vie, Montreal, Quebec, Canada. [3]Department of Physics and Astronomy, The University of Western Ontario, London, Ontario, Canada. [4]Muséum National d'Histoire Naturelle, IMPMC, Paris, France. [5]GEOPS, Université Paris-Saclay, Orsay, France. [6]PatriNat, MNHN, OFB, IRD, CNRS, Paris, France. [7]Laboratoire d'Astrophysique de Marseille, Marseille, France. [8]Naturhistorisches Museum Wien, Vienna, Austria. [9]Natural History Museum Abu Dhabi, Abu Dhabi, United Arab Emirates. [10]CEREGE, CNRS, Aix-Marseille Université, IRD, INRAE, Aix-en-Provence, France. [11]Astronomical Institute of the Romanian Academy, Bucharest, Romania. [12]International Meteor Organization, Hove, Belgium. [13]Institut Polytechnique des Sciences Avancées (IPSA), Ivry-sur-Seine, France. [14]Observatoire des Sciences de l'Univers, Institut Pythéas, Marseille, France. [15]Astronomical Institute of the Czech Academy of Sciences, Ondřejov, Czech Republic. [16]Space Science and Technology Centre and International Centre for Radio Astronomy Research, Curtin University, Perth, Western Australia, Australia. [17]NEO Coordination Centre, Planetary Defence Office, ESA, Frascati, Italy. [18]Jet Propulsion Laboratory, California Institute of Technology, Pasadena, CA, USA. [19]Konkoly Observatory, HUN-REN Research Centre for Astronomy and Earth Sciences, Budapest, Hungary. [20]Institute of Physics and Astronomy, Eötvös Loránd University, Budapest, Hungary. [21]Lowell Observatory, Flagstaff, AZ, USA. [22]Departamento de Física, Ingeniería de Sistemas y Teoría de la Señal, Universidad de Alicante, Alicante, Spain. [23]Institut de Ciències del Cosmos (ICCUB), Universitat de Barcelona (IEEC-UB), Barcelona, Spain. [24]CEA, DAM DIF, Arpajon, France. [25]Royal Netherlands Meteorological Institute, De Bilt, The Netherlands. [26]Faculty of Civil Engineering & Geosciences, Delft University of Technology, Delft, The Netherlands. [27]Inst. für Geochemie und Petrologie, ETH Zürich, Zurich, Switzerland. [28]Institut Universitaire Européen de la Mer (IUEM), University of Brest, CNRS, Ifremer, IRD, LEMAR, Plouzané, France. [29]Institut Universitaire de France, Paris, France. [30]Faculty of Mathematics, Physics and Informatics, Comenius University, Bratislava, Slovakia. [31]Faculty of Physics, Isotope Physics, University of Vienna, Vienna, Austria. [32]Faculty of Aerospace Engineering, Delft University of Technology, Delft, The Netherlands. [33]Naturalis Biodiversity Centre, Leiden, The Netherlands. [34]Agricultural University of Athens, Athens, Greece. [35]Faculty of Mathematics and Physics, Institute of Astronomy, Charles University, Prague, Czech Republic. [36]European Southern Observatory, Garching, Germany. [37]Université de Strasbourg, Strasbourg, France. [38]Schiaparelli Observatory, Varese, Italy. [39]Saint-Pardon-de-Conques Observatory, Saint-Pardon-de-Conques, France. [40]Dax Observatory, Dax, France. [41]Višnjan Observatory, Visnjan, Croatia. [42]SATINO Remote Observatory, Saint-Michel-L'Observatoire, France. [43]Astronomical Society Istra Pula, Pula, Croatia. [44]The UK Meteor Network, Tackley, UK. [45]Thüringer Landessternwarte Tautenburg, Tautenburg, Germany. [46]CNRS, IPAG, Université Grenoble Alpes, Grenoble, France. [47]Asteroid Threat Assessment Project, NASA Ames Research Center, Moffett Field, CA, USA. [48]SETI Institute, Mountain View, CA, USA. *A list of authors and their affiliations appears at the end of the paper. ✉e-mail: auriane.egal@montreal.ca

FRIPON International Team

Josep Maria Trigo-Rodriguez[49,50], Enrique Herrero[50], Jim Rowe[51], Andrew R. D. Smedley[51,52], Ashley King[51,53], Salma Sylla[54], Daniele Gardiol[55], Dario Barghini[55], Hervé Lamy[56], Emmanuel Jehin[57], Detlef Koschny[58], Bjorn Poppe[59], Andrés Jordán[60,61,62], Rene A. Mendez[63], Katherine Vieira[64], Hebe Cremades[65], Hasnaa Chennaoui Aoudjehane[66] & Zouhair Benkhaldoun[67]

[49]Institute of Space Sciences (CSIC), Barcelona, Spain. [50]Institut d'Estudis Espacials de Catalunya (IEEC), Castelldefels, Spain. [51]The UK Fireball Alliance (UKFAll), London, UK. [52]Department of Earth and Environmental Sciences, University of Manchester, Manchester, UK. [53]Natural History Museum, London, UK. [54]Université Cheikh Anta Diop Dakar-Fann, Dakar, Senegal. [55]Osservatorio Astrofisico di Torino, INAF, Pino Torinese, Italy. [56]Royal Belgian Institute of Space Aeronomy, Uccle, Belgium. [57]STAR, Space sciences, Technologies Astrophysics Research Institute, Université de Liège, Liege, Belgium.

[58]Lunar and Planetary Exploration, Technical University of Munich, Ottobrunn, Germany. [59]Division for Medical Radiation Physics and Space Environment, University of Oldenburg, Oldenburg, Germany. [60]Facultad de Ingeniería y Ciencias, Universidad Adolfo Ibáñez, Santiago, Chile. [61]Millennium Institute for Astrophysics, Santiago, Chile. [62]El Sauce Observatory-Obstech, Coquimbo, Chile. [63]Departamento de Astronomía, Universidad de Chile, Santiago, Chile. [64]Instituto de Astronomía y Ciencias Planetarias, Universidad de Atacama, Copiapó, Chile. [65]CONICET, Grupo de Estudios en Heliofísica de Mendoza, Universidad de Mendoza, Mendoza, Argentina. [66]GAIA Laboratory, Faculty of Science Ain Chock, Hassan II University of Casablanca, Casablanca, Morocco. [67]Oukaimeden Observatory, High Energy Physics and Astrophysics Laboratory, Faculty of Science Semlalia, Cadi Ayyad University, Marrakech, Morocco.

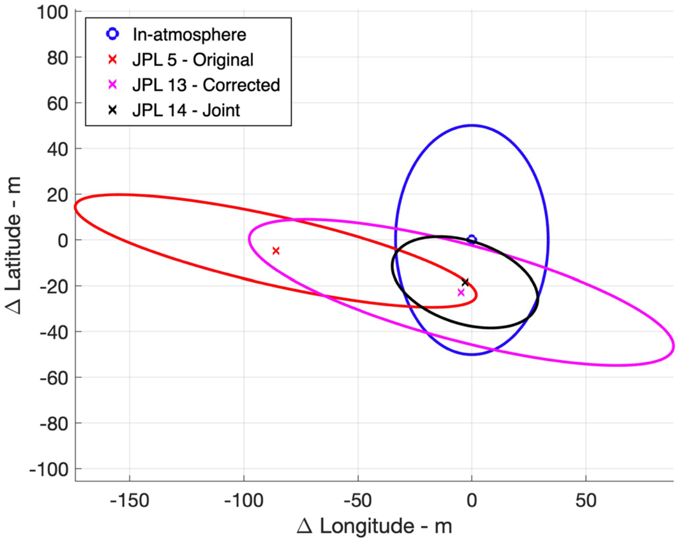

Extended Data Fig. 1 | Trajectory solutions for 2023 CX1 from telescopic and fireball data. Comparison between the position of 2023 CX1 at the top of the atmosphere as computed from ground-based astrometry and from fireball observations (blue). The selected reference altitude of 101.755 km corresponds to the first observed position of the fireball. Ellipses represent the 3σ confidence level. The initial solution (red) was calculated using altitudes of observing stations as originally reported to the MPC. An updated solution recalculated after correcting the observers' coordinates and assuming a 20 m positional uncertainty is shown in magenta. The joint solution (black) combines data from both telescopic and fireball observations.

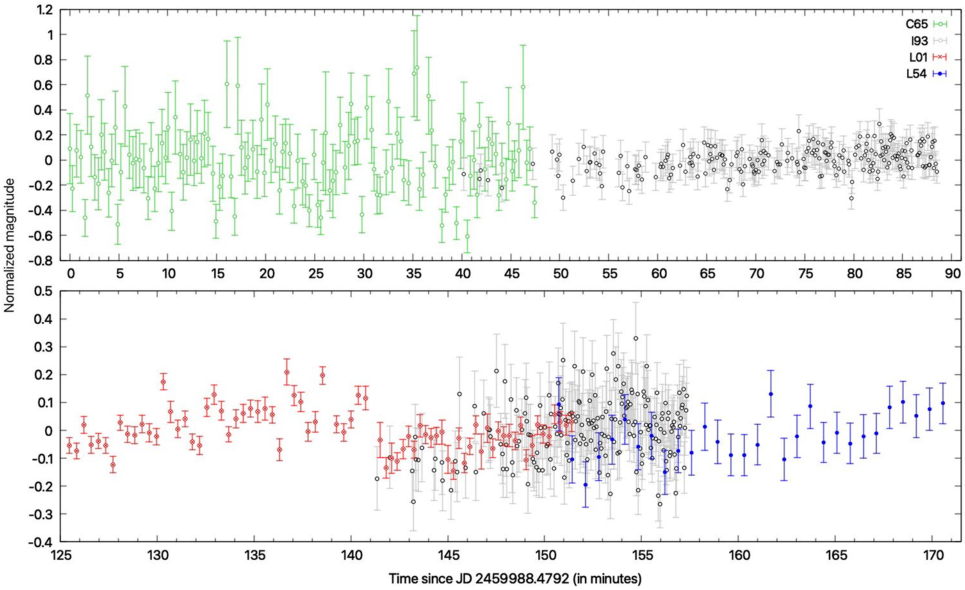

Extended Data Fig. 2 | Asteroid light curve. Asteroid brightness of 2023 CX1, starting at 23:30:02 UTC, phase angle corrected and normalized to a common distance to the asteroid, measured by the TJO (C65, green), St Pardon de Conques (I93, grey), Visjan (L01, red) and Berthelot (L54, blue) observatories. Data points represent normalized magnitudes with 1-sigma error bars derived from the photometric calibration for each individual frame (see Methods 'Asteroid photometry').

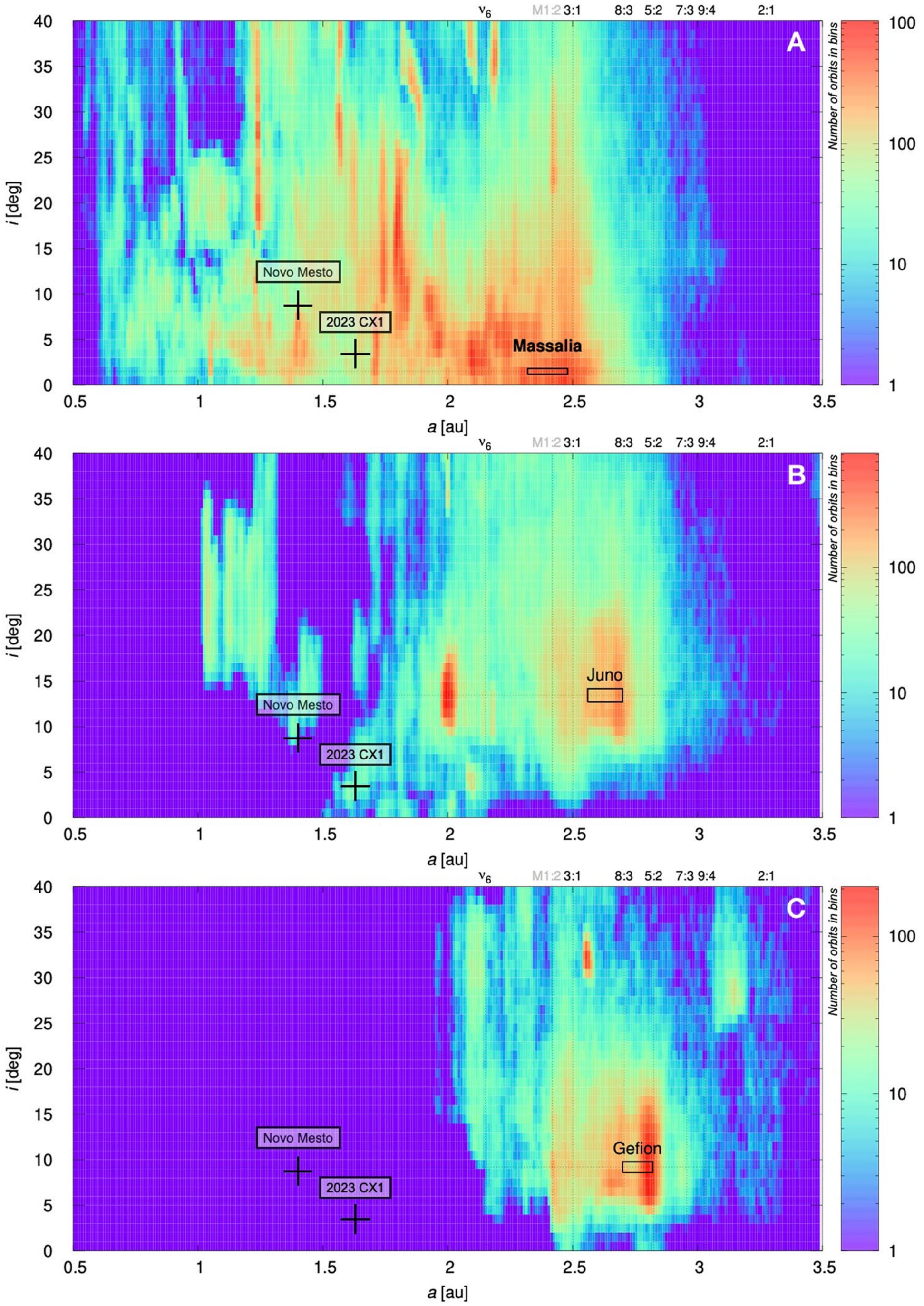

Extended Data Fig. 3 | Synthetic probability maps linking 2023 CX1 to asteroid families. Synthetic probability maps for an orbit with a given semi-major axis a and inclination i to originate from one of the L chondrite-like asteroid families: Massalia2 (**a**), Juno (**b**), and Gefion (**c**), using the METEOMOD software[21].

Extended Data Table 1 | Pre-atmospheric radius and mass of 2023 CX1

Technique / Data	Mass (kg)	Radius (cm)	Albedo p_V[1]
Asteroid magnitude	1280 ± 780	43 ± 10	(0.196 ± 0.036)[2]
Infrasound	1450 ± 850	45 ± 10	0.18 ± 0.09
Lightcurve	650 ± 160	36 ± 3	0.28 ± 0.05
Cosmogenic ^{21}Ne/^{22}Ne	≥ 370	≥ 30	≤ 0.41
^{26}Al activity (IAMS)	≥ 110	≥ 20	≤ 0.92
^{26}Al activity (GS)	470 ± 410	28 ± 12	0.47 ± 0.60
^{60}Co activity (GS)	230 ± 100	25 ± 4	0.59 ± 0.20

Estimates of the preatmospheric mass, radius, and geometric albedo (ρ_V) of 2023 CX1 derived with multiple independent methods, as detailed in Methods ‘Pre-atmospheric radius and mass’. The size to geometric albedo conversion was performed following[36], as exemplified by the asteroid with a measured absolute magnitude H of 32.7 ± 0.3. 2023 CX1 assumed geometric albedo range is based on the preferred albedo for asteroid (20) Massalia reported by the the Virtual Observatory Solar System Open Database Network[42]. Uncertainties were symmetrized by averaging the propagated upper and lower bounds. Calculations of radius assume a spherical body with a density of 3300 kg/m^3. Within uncertainties, most estimates converge toward a preatmospheric radius between 35 and 39 cm. The only exception is the estimate based on measured ^{60}Co activity via gamma spectrometry (GS), which yields a lower value, likely due to the meteoroid being too small to develop a full nucleonic cascade in its interior. A weighted average combining the estimates from asteroid photometry, fireball light curve, infrasound data, and ^{26}Al and ^{60}Co GS yields a preferred preatmospheric radius of 36 ± 3 cm and an initial mass of 650 ± 160 kg.

Extended Data Table 2 | Fragmentation details of 2023 CX1

Fragmentation location	Time (UT)	Longitude (°E)	Latitude (°N)	Height (km)
Optical (1st fragmentation)	02:59:20.10 ± 0.04 s	0.683 ± 0.00015	49.808 ± 0.00015	29.4 ± 0.01
Optical (2nd fragmentation)	02:59:20.23 ± 0.04 s	0.699 ± 0.00015	49.806 ± 0.00025	28.1 ± 0.02
Acoustic	02:59:17.4 ± 4 s	0.64 ± 0.07	49.81 ± 0.05	27.9 ± 1.0
Individual fragments	Label	Origin height (km)	Initial mass (g)	Meteorite mass (g)
	A	29.4	5500	1550
	B	28.1	960	630
	C	28.1	700	460
	D	29.4	620	400
	E	28.1	610	400
	F	34.6	300	190
	G	28.1	190	130
	H	28.1	90	60
	I	29.4	70	50

The first three rows compare the timing and locations of fragmentation events identified from optical observations of the fireball, along with an independent determination of the main fragmentation event derived from acoustic measurements (see Methods 'Seismo-acoustic analysis of the meteor'). The acoustic estimate shows good agreement with the optical results within uncertainties. The remaining rows present the separation heights and initial masses of the nine fragments identified in the video recorded from the village of La Fresnaye, along with the masses of meteorites recovered near their predicted landing sites.

Extended Data Table 3 | Atmospheric trajectory of 2023 CX1 before and after the main flare

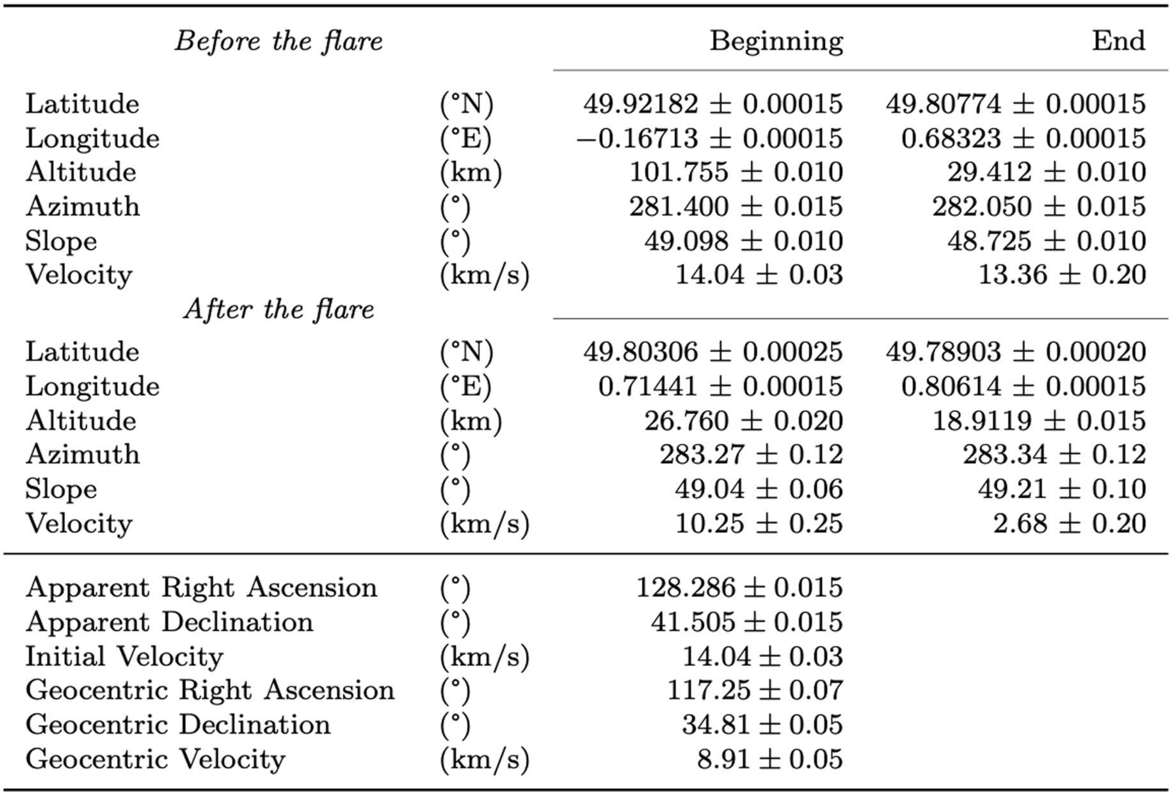

Before the flare		Beginning	End
Latitude	(°N)	49.92182 ± 0.00015	49.80774 ± 0.00015
Longitude	(°E)	−0.16713 ± 0.00015	0.68323 ± 0.00015
Altitude	(km)	101.755 ± 0.010	29.412 ± 0.010
Azimuth	(°)	281.400 ± 0.015	282.050 ± 0.015
Slope	(°)	49.098 ± 0.010	48.725 ± 0.010
Velocity	(km/s)	14.04 ± 0.03	13.36 ± 0.20
After the flare			
Latitude	(°N)	49.80306 ± 0.00025	49.78903 ± 0.00020
Longitude	(°E)	0.71441 ± 0.00015	0.80614 ± 0.00015
Altitude	(km)	26.760 ± 0.020	18.9119 ± 0.015
Azimuth	(°)	283.27 ± 0.12	283.34 ± 0.12
Slope	(°)	49.04 ± 0.06	49.21 ± 0.10
Velocity	(km/s)	10.25 ± 0.25	2.68 ± 0.20
Apparent Right Ascension	(°)	128.286 ± 0.015	
Apparent Declination	(°)	41.505 ± 0.015	
Initial Velocity	(km/s)	14.04 ± 0.03	
Geocentric Right Ascension	(°)	117.25 ± 0.07	
Geocentric Declination	(°)	34.81 ± 0.05	
Geocentric Velocity	(km/s)	8.91 ± 0.05	

Atmospheric trajectory of the fireball before and after the flare. The coordinates, including altitude, are given in the WGS84 system. The slope is given relative to the local horizon, and the velocity is given relative to the Earth surface. The brightest part of the fireball was excluded from the measurement.

Extended Data Table 4 | Summary of infrasound signal characteristics from the 2023 CX1 fireball

Station	Range (km)	Max. Amp. (Pa)	Az Dev. (degs)	Peak-to-peak amplitude (Pa)	Period at Max Amp (zero-crossing)(sec)	Period at peak PSD (sec)	Celerity (km/s)
I48TN	1701	0.04 ± 0.015	1.5	0.06 ± 0.03	1.2 ± 0.3	1.5	0.316
I26DE	941	0.25 ± 0.18	-1	0.43 ± 0.36	1.64 ± 0.03	1.8	0.321
I43RU	2507	0.05 ± 0.01	-3.2	0.08 ± 0.02	1.61 ± 0.01	1.5	0.293
I31KZ	3969	0.006 ± 0.005	-23.1	0.011 ± 0.01	2.18 ± 0.12	1.3	0.292
I46RU	5439	0.008 ± 0.006	-3.2	0.04 ± 0.012	1.83 ± 0.62	1.6	0.291
DBNI	450	0.29 ± 0.02	-	0.42 ± 0.03	0.67 ± 0.03	0.71	0.292
FLERS	145	0.40	-	0.76	1.6	1.5	-
CEA	170	2.67	-	4.24	1.4	1.37	-
AM-R9BD8	165	0.12	-	0.577	0.35	0.27	0.310
AM-R82EC	180	0.27	-	0.509	0.72	0.79	0.301
AM-RD5DB	165	0.34	-	0.616	0.37	0.36	0.296
AM-RD44E	160	0.32	-	0.954	0.25	0.34	0.314

Measurements from the Raspberry Pi Shake & Boom citizen program have preamble “AM-”.

Extended Data Table 5 | Arrival features of the seismo-acoustic signal detected by several stations in France and the United Kingdom

Station	Time	R (km)	Amp. (nm/s)	Az. (°)	Dist (km)	HDist (km)	V (km/s)	Vc (km/s)	ΔAz degs
VALM	03:01:05	28	1236	252	30.9	11.4	0.280	0.281	-0.3
GOTF	03:04:23	89	117	181	93.4	88.9	0.299	0.302	-3.2
MERIC	03:04:36	89	310	82	100.3	96.1	0.315	0.311	3.8
HARD	03:05:11	103	310	123	114.5	110.9	0.313	0.320	-8.1
FLERS	03:07:13	145	-	33.2	144.1	141.2	0.304	0.302	3.1
CLEV	03:07:29	147	413	161	153.7	151.0	0.310	0.310	-0.5
CURIE	03:08:14	-	-	-	167.7	165.3	0.317	0.310	12.1
BARI	03:09:12	188	1006	97	198.7	196.7	0.330	0.332	-4.4

Only stations used to locate the main fragmentation event are presented in the table. Listed are range (R), Peak-to-peak amplitudes (Amp.), which are read on the vertical component, Back-Azimuth (Az.), 3D Celerity model distance, corresponding horizontal distance, wave velocity, model wave velocity, calculated residual in back azimuth.

Extended Data Table 6 | Noble gas concentrations and isotopic ratios in SPLV samples

SPLV sample	#4	#10	#13	#26	#1
Sample mass [mg]	20.157±0.008	16.647±0.013	17.763±0.015	23.153±0.018	16.061±0.011
^{4}He	877.3±2.4	1228.3±3.6	1251.0±4.1	1156.0±3.8	1100.3±3.1
^{3}He/^{4}He×10^{4}	613.9±2.4	433.7±1.9	404.4±1.9	441.5±2.0	469.5±2.1
^{20}Ne	11.560±0.061	11.799±0.067	11.620±0.077	11.550±0.057	10.806±0.070
^{20}Ne/^{22}Ne	0.8392±0.0039	0.8334±0.0039	0.8360±0.0044	0.8461±0.0033	0.8374±0.0040
^{21}Ne/^{22}Ne	0.9336±0.0039	0.9335±0.0042	0.9263±0.0044	0.9332±0.0039	0.9282±0.0046
$(^{22}\mathrm{Ne}/^{21}\mathrm{Ne})_{cos}$	1.0711±0.0044	1.0713±0.0048	1.0795±0.0051	1.0716±0.0045	1.0774±0.0053
$(^{3}\mathrm{He}/^{21}\mathrm{Ne})_{cos}$	4.188±0.023	4.031±0.026	3.929±0.028	4.007±0.024	4.313±0.032
^{36}Ar	1.573±0.017	2.175±0.021	2.503±0.029	1.638±0.017	2.390±0.021
^{36}Ar/^{38}Ar	0.978±0.011	1.148±0.011	1.426±0.017	0.970±0.010	1.525±0.014
^{40}Ar/^{36}Ar	4110±55	2854±34	2649±38	3921±50	2661±31
^{84}Kr	0.789±0.019	0.578±0.022	1.007±0.021	0.648±0.016	0.630±0.023
^{78}Kr/^{84}Kr	1.06±0.14	1.57±0.24	1.317±0.099	1.88±0.11	1.48±0.32
^{80}Kr/^{84}Kr	8.52±0.52	17.77±0.82	13.99±0.54	12.39±0.60	18.8±1.0
^{82}Kr/^{84}Kr	25.2±1.4	31.6±1.7	26.7±1.1	26.2±1.0	29.1±1.3
^{83}Kr/^{84}Kr	25.37±0.99	28.4±1.4	25.82±0.69	26.6±1.1	26.6±1.6
^{86}Kr/^{84}Kr	29.4±1.3	28.1±2.0	29.82±0.86	29.7±1.5	29.8±1.9
$(^{80}\mathrm{Kr}/^{82}\mathrm{Kr})_{\mathrm{excess}}$	1.1±1.8	1.53±0.87	2.7±1.8	3.4±5.3	2.6±1.7
^{132}Xe	1.3600±0.0098	0.7225±0.0094	0.773±0.010	0.865±0.013	0.862±0.014
^{124}Xe/^{132}Xe	0.538±0.035	0.642±0.060	0.688±0.054	0.636±0.053	0.608±0.055
^{126}Xe/^{132}Xe	0.607±0.035	0.88±0.10	0.876±0.056	0.672±0.070	0.718±0.042
^{128}Xe/^{132}Xe	8.62±0.16	8.79±0.22	8.86±0.46	8.52±0.29	8.78±0.30
^{129}Xe/^{132}Xe	112.1±1.1	111.2±1.6	116.2±2.4	111.8±2.0	113.2±2.5
^{130}Xe/^{132}Xe	16.27±0.18	16.53±0.55	16.99±0.36	16.13±0.33	16.48±0.48
^{131}Xe/^{132}Xe	81.72±0.74	83.4±1.6	84.5±1.9	80.9±1.3	82.8±2.2
^{134}Xe/^{132}Xe	38.99±0.49	39.5±1.0	40.19±0.95	38.85±0.82	38.30±0.84
^{136}Xe/^{132}Xe	33.06±0.39	33.58±0.96	34.06±0.80	32.21±0.73	31.2±1.1

He, Ne, Ar, Kr, Xe concentrations and isotopic ratios. He, Ne, Ar concentrations are given in 10^{-8} cm^{3} STP/g, Kr and Xe concentrations are provided in 10^{-10} cm^{3} STP/g. Shielding-dependent measured cosmogenic isotope ratios are also provided. Values of ^{84}Kr=100 and ^{132}Xe=100 were used for the ratios.

Extended Data Table 7 | Cosmogenic and radiogenic isotopes, elemental concentrations, and exposure ages of SPLV samples

Sample	$^{3}\mathrm{He}_{cos}$ $10^{-8}\mathrm{cm}^3$ STP/g	$^{21}\mathrm{Ne}_{cos}$ $10^{-8}\mathrm{cm}^3$ STP/g	$^{38}\mathrm{Ar}_{cos}$ 10^{-8} cm^3 STP/g	Radius^1 cm	Depth cm
SPLV #4	53.86 ± 0.15	12.860 ± 0.061	1.493 ± 0.027	35-50	21-40
SPLV #26	51.04 ± 0.16	12.739 ± 0.065	1.568 ± 0.027	35-50	21-40
SPLV #13	50.59 ± 0.17	12.876 ± 0.079	1.461 ± 0.031	30-50	15-35
SPLV #10	53.28 ± 0.18	13.216 ± 0.072	1.689 ± 0.028	35-50	21-40
SPLV #1	51.66 ± 0.18	11.977 ± 0.078	1.271 ± 0.022	30-50	16-37

Sample	P_3 $10^{-8}\mathrm{cm}^3/(\mathrm{g}^*\mathrm{Myr})$	P_{21} $10^{-8}\mathrm{cm}^3/(\mathrm{g}^*\mathrm{Myr})$	P_{38} $10^{-8}\mathrm{cm}^3/(\mathrm{g}^*\mathrm{Myr})$	T_3 Myr	T_{21} Myr	T_{38} Myr	T_{26} Myr
SPLV #4	1.93-2.03	0.42-0.44	0.045-0.046	26-28	29-31	32-34	29 ± 6
SPLV #26	1.93-2.03	0.42-0.44	0.045-0.046	25-26	29-30	33-36	30 ± 6
SPLV #13	1.91-2.03	0.40-0.44	0.043-0.046	25-27	29-32	31-35	30 ± 6
SPLV #10	1.93-2.03	0.42-0.44	0.045-0.046	26-28	30-32	36-39	32 ± 9
SPLV #1	1.91-2.03	0.41-0.44	0.043-0.046	25-27	27-30	27-30	30 ± 6

Sample	$^{4}\mathrm{He}_{rad}$ $10^{-8}\mathrm{cm}^3$ STP/g	$^{40}\mathrm{Ar}_{rad}$ $10^{-8}\mathrm{cm}^3$ STP/g	K^2 ppm	U^2 ppb	Th^2 ppb	T_4 Gyr	T_{40} Gyr
SPLV #4	573 ± 24	6370 ± 140	830	13	43	1.8-1.9	4.4-4.5
SPLV #26	868 ± 23	6330 ± 140				2.5-2.6	4.4-4.5
SPLV #13	965 ± 23	6400 ± 260				2.7-2.8	4.4-4.6
SPLV #10	927 ± 24	6050 ± 190				2.6-2.8	4.3-4.4
SPLV #1	808 ± 23	6130 ± 250				2.4-2.5	4.3-4.5

Cosmogenic and radiogenic isotope concentrations, K, U, Th concentrations, shielding conditions (preatmospheric meteoroid radius and sample depth within the meteoroid), production rates P_x, cosmic ray exposure ages T_x, and U/Th-He and K-Ar gas retention ages T_x. T_{26} ages were determined from the ^{26}Al-^{21}Ne isotope pair method (cf. Methods 'Gamma spectrometry'). The bulk chemical composition determined for SPLV #1 via ICP-AES/ICP-MS (see Supplementary Table 3) was applied to all samples. An upper radius limit of 50 cm was set from fireball observations.